5-2017

Solar Wind-Magnetosphere Coupling: A Global Perspective of Reconnection in the Magnetotail

Miles Thomas Bengtson

SOLAR WIND-MAGNETOSPHERE COUPLING: A GLOBAL PERSPECTIVE OF RECONNECTION IN THE MAGNETOTAIL

By
Miles Thomas Bengtson

A Thesis Submitted to the Physical Sciences Department In Partial Fulfillment of the Requirements for the Degree of Master of Science in Engineering Physics

Embry-Riddle Aeronautical University
Daytona Beach, Florida
May 2017

SOLAR WIND-MAGNETOSPHERE COUPLING: A GLOBAL PERSPECTIVE OF RECONNECTION IN THE MAGNETOTAIL

by

Miles Thomas Bengtson

This thesis was prepared under the direction of the candidate's thesis committee chair, Dr. Katariina Nykyri, Department of Physical Sciences, and has been approved by the members of the thesis committee. It was submitted to the Department of Physical Sciences and was accepted in partial fulfillment of the requirements of the Degree of Master of Science in Engineering Physics

THESIS COMMITTEE:

Dr. Katariina Nykyri, Chair

Dr. Anatoly Streltsov, Member

Dr. Kshitija Deshpande, Member

Dr. Alan Liu, MSEP Graduate Program Coordinator

Dr. Terry Oswalt, Department Chair, Physical Sciences

Dr. Christopher Grant, Vice Chancellor

Abstract

We present a case study of the 25 December 2015 substorm which occurred between 08:15 and 08:45 Universal Time. During this interval, fast particle flows and field geometry consistent with magnetic reconnection were detected in the mid-tail region. An ejected plasmoid was observed by the lunar-orbiting Acceleration, Reconnection, Turbulence and Electrodynamics of Moon's Interaction with the Sun (ARTEMIS) probes and corresponding dipolarization signature was observed by the Time History of Events and Macroscale Interactions During Substorms (THEMIS) spacecraft earthward of the reconnection site, which was determined to be approximately -33 R_E. Ground signatures indicative of substorm activity were also observed by the THEMIS ground-based observatories during this interval. Prior to the substorm, none of the solar-wind monitoring missions (Geotail, OMNI, ACE) observed a significant southward B_z which could have initiated the event. The Magnetospheric Multiscale (MMS) spacecraft, which were in the dayside magnetosheath, detected a strong pulse in B_z, with a minimum near -35 nT, at ∼08:05 UT, consistent with the time delay required for propagation from the magnetosheath to the mid-tail. We propose that this pulse is either a small-scale structure in the solar wind, the result of a kinetic shock process due to a solar wind discontinuity hitting the bow shock, or a flux-transfer event at the magnetopause and, further, that this strong southward component of B_z in the magnetosheath is associated with the trigger of the observed substorm. We simulate the entire magnetosphere in maximum detail for this

event using the Space Weather Modeling Framework/Block Adaptive Tree Solar-wind Roe Upwind Scheme (SWMF/BATS-R-US) model from NASA's Community Coordinated Modeling Center (CCMC) with a special, high-resolution grid. The results of this work will be highly relevant to future solar wind observation missions, global-scale magnetohydrodynamic models, and the ongoing effort to understand how processes at lunar distances in the tail couple to the rest of the near-Earth space environment.

Acknowledgments

We acknowledge NASA contract NAS5-02099 and V. Angelopoulos for use of data from the THEMIS Mission. Specifically: D. Larson and R. P. Lin for use of SST data, C. W. Carlson and J. P. McFadden for use of ESA data, K. H. Glassmeier, U. Auster and W. Baumjohann for the use of FGM data provided under the lead of the Technical University of Braunschweig and with financial support through the German Ministry for Economy and Technology and the German Center for Aviation and Space (DLR) under contract 50 OC 0302, S. Mende and E. Donovan for use of the ASI data, the CSA for logistical support in fielding and data retrieval from the GBO stations, and NSF for support of GIMNAST through grant AGS-1004736, S. Mende and C. T. Russell for use of the GMAG data and NSF for support through grant AGS-1004814. Data provided by the Geophysical Institute Magnetometer Array operated by the Geophysical Institute, University of Alaska. More information about this dataset is available at: http://magnet.asf.alaska.edu/.

MMS development and operations work at JHU/APL, UCLA, UNH, GSFC, and SwRI was supported by NASA contract NNG04EB99C. MMS data are available from the MMS Science Data Center website:

https://lasp.colorado.edu/mms/sdc/.

Geotail magnetic field and plasma data were provided by T. Nagai (H. Hayakawa and/or Y. Saito) through DARTS at Institute of Space and Astronautical Science, JAXA in Japan. Data are available at:

https://darts.isas.jaxa.jp/stp/geotail/.

Simulation results have been provided by the Community Coordinated Modeling Center at Goddard Space Flight Center through their public Runs on Request system (http://ccmc.gsfc.nasa.gov). The CCMC is a multi-agency partnership between NASA, AFMC, AFOSR, AFRL, AFWA, NOAA, NSF and ONR. The SWMF/BATSRUS Model was developed by the Center for Space Environment Modeling at the University of Michigan.

Contents

List of Tables

List of Figures

Chapter 1

Introduction

1.1 Motivation and Goals

The purpose of this research is to achieve a more complete understanding of magnetospheric substorms on a global scale. Many previous studies have focused on substorm phenomena in individual regions, such as ionospheric processes, timing analysis in the near-Earth tail, and pre-substorm solar wind characteristics. Significant advancements in these areas have been made in recent years due to the ongoing operation of a number of spacecraft missions, including THEMIS, MMS, and Cluster, in addition to the establishment of a dense ground observation network throughout North America and Greenland. The THEMIS, mission, for example, recently determined which substorm model most accurately agrees with the data, documenting the time history and onset location for a number of substorms. Despite this progress, however, many questions remain regarding how substorm processes in the near-tail and ionosphere couple to the other magnetospheric regions and a global-scale timeline of substorm events has not been fully established. Considering that substorms are one of the most regular events in which energy is stored and released in the geospace environment, it is critical that the science community achieve a full understanding of substorm physics, eventually de-

veloping predictive capabilities on global and local levels. For this reason, the National Science Foundation Geospace Environment Modeling (GEM) program has established focus groups on Tail-Inner Magnetosphere Interactions (2012-2016), Magnetic Reconnection in the Magnetosphere (2013-2017), and Tail Environment and Dynamics at Lunar Distances (2015-2019). This thesis addresses several topics highly relevant to each of these focus groups, which together represent some of the most important topics at the forefront of space physics. The work presented herein discusses a substorm case study using observations from each major area of the near-Earth space environment: the solar wind, magnetosheath, near and far-tail, and ionosphere. The observations span over 80 R_E (Earth radii) in space and ∼90 minutes in time and use data from six spacecraft missions for a single substorm which occurred on 25 December 2015 between 08:00 and 08:30 UT. In addition, global magnetohydrodynamic codes are used to model the magnetosphere during this event. Our primary goal in this study is to determine a time history of events all the way from the initial growth phase to the ultimate energy dissipation and to examine how different regions of the geospace environment couple with each other. The results of this work will have important implications for future solar wind monitoring missions and global-scale space weather modeling efforts.

1.2 The Geomagnetic Environment

The magnetosphere describes the region around the Earth in which the magnetic field generated by the Earth dominates the interplanetary magnetic field (IMF) which is generated by the sun. The near-Earth space environment can be thought of as a system of systems, in which each unique region has well-defined boundaries, dominant physical processes, and characteristic temporal and spatial scales. The energy released by the sun in the form of the highly dynamic solar wind, a magnetized plasma which flows outward

from the sun through the solar system, is what drives the entire system. The transport of mass, momentum, and energy from the sun through the various regions of the magnetosphere via numerous physical processes is known as space weather. Space weather can be considered as an analog of weather on Earth. Both can have a large effect on our daily lives and, oftentimes, can cause significant damage to humanity's critical infrastructure and even loss of life. For this reason, one crucial scientific goal of our time is to achieve an understanding of space weather and develop the ability to predict space weather with an accuracy comparable to that of atmospheric weather. This endeavor involves studying the physics of each individual region of the heliosphere and magnetosphere, as well as the mechanisms through which they interact. Figure 1.1 shows a diagram of the magnetosphere, illustrating the most important regions.

Regions of the magnetosphere which are relevant to this study include the bow shock, dayside magnetosheath, magnetopause, magnetotail, neutral sheet, and polar ionosphere. The bow shock is the initial (furthest upstream) boundary at which the solar wind interacts with the Earth's magnetic field. At this boundary, the solar wind transitions from supersonic to subsonic flow, forming a standing wave in front of the Earth, with a typical stand-off distance of approximately 15 R_E in the Geocentric Solar Magnetospheric (GSM) coordinate system (*Fairfield*, 1971). The orientation of the IMF at this boundary drives many of the processes around the Earth. The magnetic field can be quasi-parallel, meaning in the same direction as the shock normal, or quasi-perpendicular, meaning at an angle of 90° with the shock normal. Whether the IMF is directed upward (North) or downward (South) is critically important to substorm physics. Next is the magnetosheath, bounded by the bowshock on the upstream side and the magnetopause (the furthest closed magnetic field line from the Earth) on the earthward side. The shocked magnetosheath plasma is hotter and denser and the magnetic field stronger than in the solar wind. The distance from the Earth to the magnetopause is

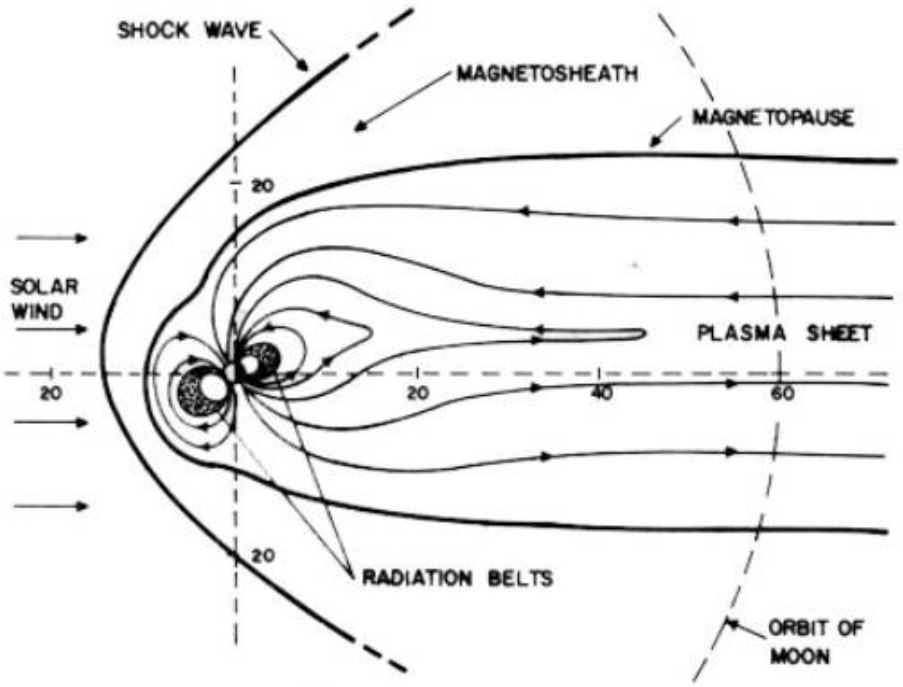

Figure 1.1: 2-D schematic of the magnetosphere denoting the locations and names of primary regions. Image available from *Platino and Inan* (2001).

determined by the balance between the solar wind total pressure, dominated by the dynamic pressure,

$$P_{dyn} = \rho v^2, \tag{1.1}$$

and the total pressure of the Earth's magnetosphere, which is dominated by the magnetic pressure,

$$P_{mag} = \frac{B^2}{2\mu_0}. \tag{1.2}$$

This distance is highly variable, but has a typical value of approximately 11 R_E (X-GSM) (*Fairfield*, 1971). Within the magnetopause, the magnetic field is dominated by the dipole-like field of the Earth. It is important to note

that the magnetic field lines emerge from the south pole and terminate at the north pole. Thus, at the dayside equatorial plane, they are directed primarily northward, antiparallel to the incoming field when IMF is southward. This condition is important for reconnection to occur at the dayside magnetopause and will be discussed in detail later.

Downstream of the Earth is the magnetotail. In this region, the dipole field becomes stretched out, forming a tail structure which reaches out to distances $> 200\ R_E$ (*Slavin et al.*, 1983). The north and south lobes of the tail are separated by the plasma sheet, the region formed by closed-field lines near the equatorial magnetotail. A current sheet (also known as the neutral sheet) is embedded within the center of the plasma sheet containing the cross-tail current, a branch of the magnetospheric current system which flows from dawn to dusk. The magnetic field is directed oppositely on either side of the current sheet (tailward in the south lobe and earthward in the north lobe). This fact is important because antiparallel field lines are a necessary condition for reconnection to occur, as will be discussed later. A neutral point (also known as an X-line) exists where the antiparallel field lines merge, thus creating field lines which are closed with respect to the Earth. Reconnection takes places at such a neutral point. Finally, the field lines in the neutral sheet (at varying distances) map to the auroral zones of the ionosphere, indicating that auroral particles are energized in this region.

1.3 Magnetic Reconnection

Magnetic reconnection is the physical process at the heart of the substorm phenomenon. The earliest discussions of magnetic reconnection occurred in the context of solar flare observations in the 1940s. *Giovanelli* (1947) proposed that magnetic energy in sunspots can be dissipated into a current at a neutral point in the magnetic field. *Dungey* (1950) first used the phrase "reconnection" to describe the change in magnetic field topology near a neu-

tral point and suggested this effect occurs is responsible for coupling between planetary magnetospheres and the solar wind. Later work by *Parker* (1957) and *Sweet* (1958) developed the first quantitative model which became widely known as the Sweet-Parker model. Though this model accurately captures the general behavior, it predicts the reconnection would occur on the order of months, whereas reconnection in physical plasmas are known to occur on the order of seconds or minutes. *Petschek* (1964) proposed an alternative to the Sweet-Parker model in which dispersive waves at small scales create a much smaller reconnection region and allow for it to occur on realistic timescales. The Petschek model thus introduced the X-line field geometry commonly used to describe a reconnection site in two dimensions. This model, however, predicts shocks separating the inflow and outflow regions, the evidence of which has not been found. The physics of magnetic reconnection remain an area of active research, though two mechanisms have been proposed which could address the reconnection rate issue: collisionless reconnection and anomalous resistivity.

To understand the reconnection physics more fully, consider the governing equation for current density in a two-species, magnetized fluid. A perfectly conducting plasma obeys the ideal Ohm's Law:

$$\mathbf{E} + \mathbf{v} \times \mathbf{B} = 0, \tag{1.3}$$

where $\mathbf{E}$ is the electric field, $\mathbf{v}$ is the plasma velocity, and $\mathbf{B}$ is the magnetic field. This equations states that if two parcels of plasma are connected by a magnetic field line, they will forever remain connected and the magnetic topology is preserved. This is known as the "frozen-in" condition because the magnetic field is frozen into the plasma. Plasma in the solar wind and magnetosphere generally satisfies this condition. In order to break the frozen-in condition and allow the magnetic field to disconnect and reconnect, a

Generalized Ohm's Law must be considered:

$$\mathbf{E}+\mathbf{v}\times\mathbf{B}=\frac{m_e m_i}{e^2\rho}\left[\frac{\partial\mathbf{J}}{\partial t}+\nabla\cdot(\mathbf{vJ}+\mathbf{Jv})\right]-\frac{m_e+m_i}{e\rho}\nabla\cdot\mathbf{P_e}+\frac{mi}{e\rho}\mathbf{J}\times\mathbf{B}+\eta\mathbf{J}, \tag{1.4}$$

where $\mathbf{J}$ is the current density, e is the elementary charge, m_e and m_i are the electron and ion masses, $\mathbf{P_e}$ is the electron pressure tensor, and η is the resistivity. The left-hand term represents the electric field in the moving plasma frame. The first term on the right-hand side represents the electron inertia, the second term represents electric fields due to gradients in the pressure tensor, the next term is the Hall term which represents ion and electron decoupling, and the final term represents the resistivity.

Simulations have shown that only the electron inertial term, off-diagonal components of the electron pressure tensor, and resistivity terms can break the frozen-in condition and allow the magnetic topology to change. For scale sizes much larger than the ion inertial length, which is given by,

$$\delta_i=\frac{c}{\omega_{pi}}, \tag{1.5}$$

where c is the speed of light and ω_{pi} is the ion plasma frequency, all of the terms on the right-hand side are approximately equal to zero and the frozen-in condition is satisfied. Strong ion-electron streaming near the X-line could drive turbulence in the form of waves, enhancing the ion-electron drag and creating unusually high or anomalous resistivity, thus breaking the frozen-in condition.

The Hall term and the pressure term of the Generalized Ohm's Law become non-zero at scales less than the ion inertial length (about 700 km in the plasma sheet). At this scale, known as the ion diffusion region, the ions become demagnetized and decouple from the motion of the electrons. The electrons continue flowing inward to the X-line, still frozen-in to the magnetic field. To fully break the frozen-in condition, the electrons must also become

demagnetized, which occurs in the much smaller electron diffusion region, characterized by the electron inertial length (about 20 km in the plasma sheet),

$$\delta_e = \frac{c}{\omega_{pe}}. \tag{1.6}$$

This scheme is known as collisionless reconnection. (e.g., *Biskamp et al.*, 1995). A Geospace Environment Modeling reconnection challenge indicated that the Hall term makes reconnection fast, as long as there is a term present which can also break the frozen-in condition at the electron scales (*Birn et al.*, 2001). In-situ observations made from within the ion diffusion region in the magnetotail strongly support this description (*Øieroset et al.*, 2001) and it is thought that collisionless effects are dominant in the magnetosphere. Figure 1.2 shows a 2-dimensional representation of a typical reconnection geometry in the magnetosphere.

Though collisionless effects at the ion scales are thought to determine the reconnection rate, the ultimate processes which break the frozen-in condition at the electron scales are unknown. The Magnetosperic Multiscale mission (MMS), a constellation of four satellites launched in 2015, was designed to take high time resolution data to investigate the microscale physics of reconnection (*Burch et al.*, 2016). A variable spacecraft separation range from 10 - 400 km will allow for multipoint measurements within both the ion and electron diffusion regions. This ongoing mission represents the cutting edge endeavors to understand reconnection. It is important to note that whereas a consideration of reconnection in two dimensions results in coherent, magnetic island structures, a three dimensional consideration of the field geometry is much more complex. For example, the X-point is in reality extended as an X-line, and the closed magnetic islands are complex, interconnected flux-rope structures. Magnetospheric reconnection is conventionally considered with the 2-D simplification, though this may neglect important physics occurring in the third dimension. The following section discusses the role which magnetic reconnection plays in the substorm phenomenon.

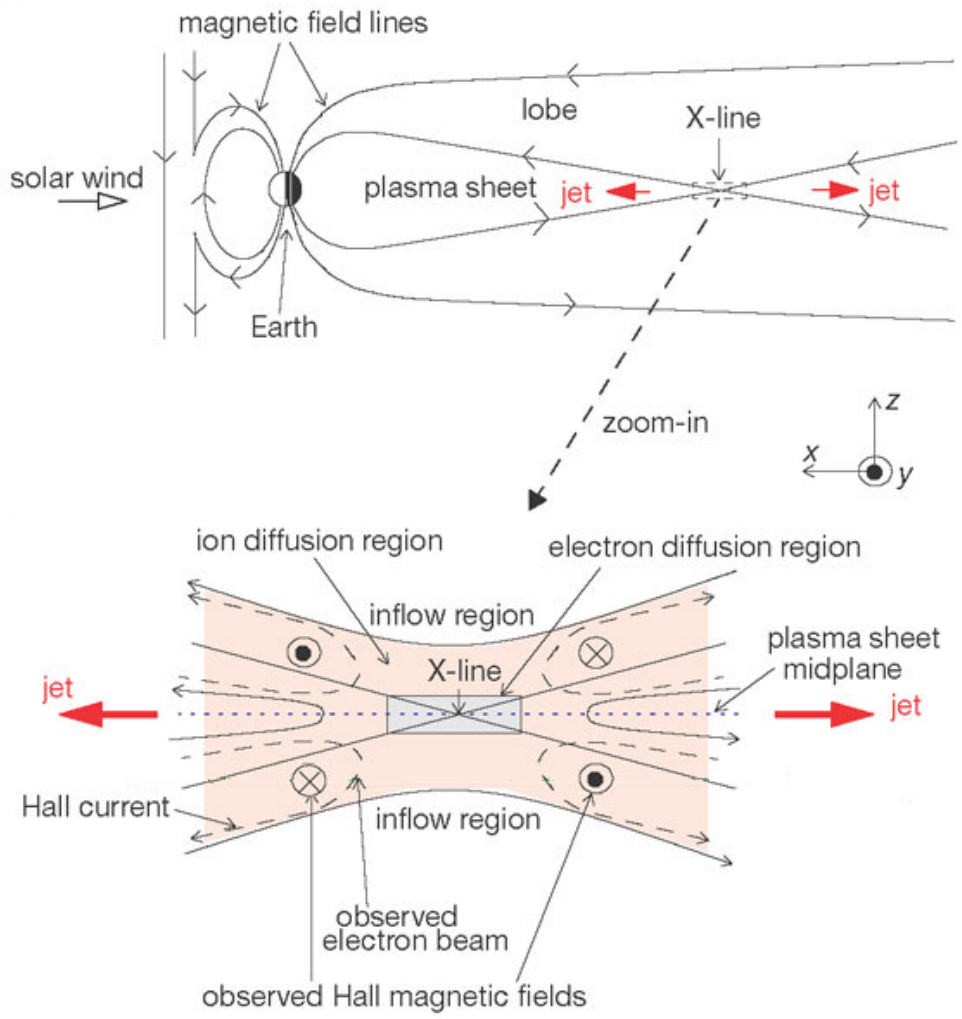

Figure 1.2: 2-D schematic of the magnetosphere (upper panel), showing reconnection sites in the dayside and tail regions. The zoomed in view (lower panel) shows several important regions around the magnetic reconnection site. Image adapted from *Øieroset et al.* (2001).

1.4 Substorms

Substorms occur when magnetic energy stored in the Earth's magnetotail is suddenly released into particle thermal or kinetic energy and the global magnetic field becomes reconfigured (*Akasofu*, 1964; *Axford*, 1999). Signatures associated with substorms include intensification and expansion of the auroral arc, an increase in the ionospheric electroject, and particle injections into the ionosphere and magnetosphere. Substorms are one of the most regular and frequent transient events observed in geospace, so achieving a solid understanding of the underlying physics is critical to understanding the magnetosphere in general. *Borovsky et al.* (1993) report that about 1500 substorms occur per year, with about half occurring in periodic intervals having an average time between substorm onsets of 2.75 hours. Other studies have shown an occurrence rate of substorm related phenomena of one event per 3.9 hours (*Fu et al.*, 2012).

1.4.1 Substorm Energy Loading: Solar Wind-Magnetosphere Coupling

The energy released in the substorm originates in the coupling of the solar wind with the magnetosphere (*Dungey*, 1961; *Baker et al.*, 1997). The coupling is particularly strong during prolonged periods of southward interplanetary magnetic field (IMF) (*Nishida*, 1983; *Rostoker et al.*, 1980; *Caan et al.*, 1977). This ensures that the field lines of the solar wind are directed anti-parallel to the closed dipole field lines of the Earth, allowing reconnection to occur on the dayside. The newly opened field lines then propagate tailward, storing energy in the form of magnetic flux in the tail regions (the growth phase of the substorm).

1.4.2 Substorm Energy Release: Magnetic Reconnection in the Tail

Ionospheric Phenomena

Substorms are closely linked to a number of ionospheric phenomena which can be detected from the ground. These phenomena include sudden intensification and expansion of the aurora (*Akasofu*, 1964), a sharp increase in the the auroral electrojet (AE) index, and magnetic field pulsations associated with substorm-generated ionospheric currents (*Saito*, 1969). Fluctuations in this current system are detected as pulsations in the ground magnetic field in the 40-150 sec range, known as Pi2 pulsations (*Saito*, 1969). Figure 1.3 shows how magnetic field fluctuations on the ground are caused by processes in the tail.

Magnetotail Phenomena

Until recently, the trigger mechanism for substorm onset was under debate. The two main models included the current sheet disruption model (*Lui*, 1996) and the Near-Earth Neutral Line (NENL) model (*McPherron et al.*, 1973; *Baker et al.*, 1996). The disruption model proposes that substorm onset is triggered by a thinning of the current sheet in which whistler waves are produced by ion-electron interactions at around 10 R_E. These waves cause the plasma sheet to act resistively, thereby disrupting the cross-tail current and diverting it through the ionosphere. This model asserts a substorm onset location much closer to the earth (10 R_E) than the NENL model. According to the Near-Earth Neutral Line model, field lines which have become stretched by the accumulation of magnetic flux in the tail reconnect at a downtail distance of 20 - 40 R_E, thereby triggering the release of energy. Plasma in the plasma sheet boundary layer above or below the X-line region flows toward the reconnection site. The plasma in the neutral sheet near the reconnection site is heated and accelerated, flowing earthward on the earthward side

of the reconnection site and tailward on the tailward side. Subsequently, a dipolarization front, or rapid increase in the north-south magnetic field component (B_z) (*Runov et al.*, 2009a), propagates earthward from the reconnection site. The earthward flows interact with the near-Earth currents, creating a circuit through the ionosphere known as a substorm current wedge (SCW) (*Atkinson*, 1967). The SCW couples the magnetospheric processes to the ionosphere, producing auroral intensifications and Pi2 pulsations. A plasmoid, or magnetic loop containing heated, confined plasma, is launched tailward along the neutral sheet toward the Distant Neutral Line in what is often termed a nightside flux transfer event (NFTE) (*Richardson and Cowley*, 1985; *Sergeev et al.*, 1992; *Ieda et al.*, 1998).

The goal of the Time History of Events and Macroscale Interactions During Substorms (THEMIS) mission (*Angelopoulos*, 2009) was to determine which of these two models is supported by evidence and to establish a timeline of substorm events for different regions of the magnetosphere. The initial mission consisted of five identical probes in orbits that aligned in major conjunctions along the Earth-Sun line every four days, allowing simultaneous multipoint measurements to be taken throughout the expected substorm initiation region of -10 R_E to -30 R_E. Additionally, a dense array of magnetometer and all-sky imager stations were deployed across Canada and Alaska to establish timing of substorm ground phenomena. THEMIS observations have recently established that substorms are triggered by reconnection which occurs at around 20 R_E downtail (*Angelopoulos*, 2009; *Liu et al.*, 2009; *Gabrielse et al.*, 2009; *Pu et al.*, 2010), as predicted by the NENL model. Further, observations have shown there is a propagation time of approximately 2-3 minutes between reconnection and auroral signatures and Pi2 pulsations being observed on the ground.

In this paper, we present observations of a substorm on 25 December 2015 in which a dipolarization front and plasmoid were observed in the near and far magnetotail, respectively. This study differs from previous timing

case studies, however, in that we consider the dayside events in detail along with the tail observations, thus establishing a timeline of events which includes disturbances in the solar wind, dayside magnetosheath, near-Earth and far-tail regions, and ionosphere. A fortuitous alignment of several independent spacecraft missions (THEMIS/ARTEMIS, MMS, and Geotail) near the Earth-Sun line allows a comprehensive analysis of the global magnetosphere during a substorm event. Considering that the ARTEMIS probes cross the tail region during only several days per month, it is unique to have multipoint measurements spanning nearly 80 R_E from upstream of the bowshock to the far-tail. In Section 2.2, we discuss observations and timing analysis from the THEMIS and ARTEMIS missions. In Section, 2.3, we discuss the ionospheric signatures and phenomena associated with the substorm. We discuss in Section 2.4 the coupling of the solar-wind and dayside magnetosheath physics with the substorm processes in the tail using data from Geotail and Magnetospheric Multiscale (MMS). Finally, we present results from global-scale MHD simulations in Section 3.

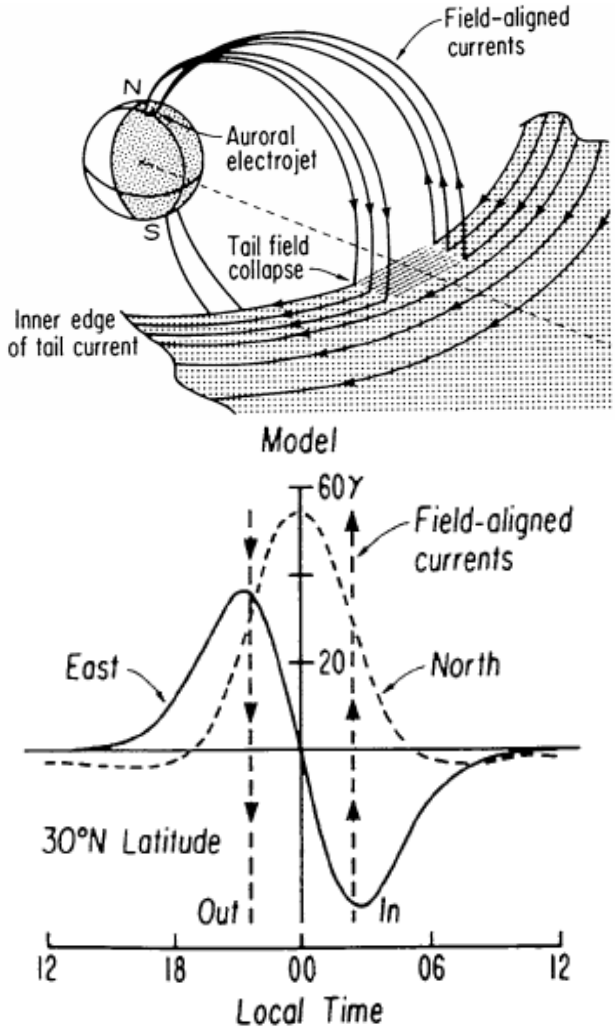

Figure 1.3: (upper) Schematic of the substorm current wedge which couples ionospheric currents to tail currents when the cross-tail current is disrupted during a reconnection event. (lower) Schematic of variations in the ground magnetic field produced by the substorm current wedge. The field strength in the north direction should be enhanced and the field strength in the east direction should decrease (increase) on the eastern (western) side of the wedge. Images originally published in *McPherron et al.* (1973).

1.5 Instrumentation

In this study, we use data from the THEMIS, ARTEMIS, MMS, and Geotail missions. Table 2.1 and Figure 2.1 provide the location of each spacecraft at 0815 UT on 25 December 2015 along with field line traces from the Tyganenko 89 model (*Tsyganenko*, 1989). Data throughout is presented in Geocentric Solar Magnetospheric (GSM) coordinates. All times are in Universal Time (UT).

1.5.1 THEMIS and ARTEMIS

The Time History of Events and Macroscale Interactions during Substorms (THEMIS) mission was launched on February 12, 2007 to determine the onset mechanism and macro-scale evolution of substorms (*Angelopoulos*, 2009). The original mission consisted of five identical micro-satellites (probes) which regularly aligned in the tail at different distances along the X-GSM axis. Perigees for each probe were $\sim$1 R_E and apogees ranged from 10 R_E for the inner probe to 30 R_E for the outer probe. This design provided multipoint measurements at key points in the near-Earth magnetotail which allowed for determination of the substorm onset region, and subsequent identification of reconnection as the substorm trigger. The THEMIS probes are officially named with letters A, B, C, D, and E, though they are generally referred to as probes P5, P1, P2, P3, and P4, respectively.

The two Acceleration, Reconnection, Turbulence, and Electrodynamics of the Moon's Interaction with the Sun (ARTEMIS) probes were originally part of the five spacecraft THEMIS mission. In 2010, the two outermost THEMIS probes, P1 and P2, were transferred to lunar orbit, thus commencing the ARTEMIS mission, while THEMIS P3, P4, and P5 remain in the near-Earth magnetosphere (*Angelopoulos*, 2011). The primary ARTEMIS objective is to study the processes which occur as the moon interacts with the pristine solar wind. During approximately three days per month, corresponding to the

full moon phase, the ARTEMIS spacecraft cross the magnetotail at ∼60 R_E. During this time, ARTEMIS observations complement the ongoing THEMIS mission by providing observations of particle acceleration and turbulence in the tail over very large probe separations.

Each of the probes is equipped with a suite of instruments to measure the electric and magnetic field and plasma properties. Observations presented in this thesis use particle data from the Electrostatic Analyzer (ESA) (*McFadden et al.*, 2008) and Solid State Telescope (SST) (*Angelopoulos*, 2009) and field data from the Fluxgate Magnetometer (FGM, 1/8 s) (*Auster et al.*, 2009). The ESA instrument obtains separate ion and electron 3-D distribution functions at a time resolution of 3 seconds (equivalent to the probe spin period). The energy range is 5 eV to 25 keV for both ions and electrons. Distribution functions are downlinked and the moments are computed on the ground to obtain the final data product. The SST instrument also produces one 3-D distribution function each spin period for ions and electrons in the energy range from 30 keV to 1 MeV.

The FGM instrument measures the magnetic field from DC to 64 Hz with an an exceptional sensitivity of 0.01 nT at cadence of 1/16 seconds. We also use data from the twenty THEMIS ground-based all-sky imagers (*Russell et al.*, 2008) and thirty-plus magnetometers arrayed across North America (*Mende et al.*, 2009a). The ASI stations take images every 3 seconds and the magnetometers measure the magnetic field vector every 1/2 seconds.

1.5.2 MMS

The Magnetospheric Multiscale (MMS) mission is a four-spacecraft constellation which was launched on March 12, 2015 (*Burch et al.*, 2016). The primary science objective of MMS is to determine what caused magnetic field lines to reconnect in a collisionless plasma. MMS collects data at high time resolution and varying spatial scales in the two magnetospheric regions where reconnection primarily occurs: the dayside magnetopause and tail re-

gion ∼25 R_E. Each of the four probes are equipped with an identical set of plasma and field instruments. We use particle data from the Fast Plasma Investigation (FPI) (*Pollock et al.*, 2016) and field data from the Fluxgate Magnetometer (*Russell et al.*, 2014; *Torbert et al.*, 2016). FPI collects 3-D distribution functions for ions and electrons from 10 eV to 30 keV at a cadence of 4.5 seconds. FGM measures fluctuations in the magnetic field from DC to 64 Hz at a cadence of 1/16 seconds. This study is primarily interested in the macroscale physics of substorm formation and evolution, so we utilize data from only one of the MMS probes to obtain data from the dayside magnetosheath. The four probes were in a tight formation during the interval of interest.

1.5.3 Geotail

The Geotail mission consists of a single spacecraft launched on July 24, 1992. The satellite was developed by the Institute of Space and Astronautical Science of Japan, launched by NASA, and carries instruments from both organizations. Geotail's primary objective has been to understand the physics of plasma acceleration in the magnetotail and the influx of solar energy into the magnetosphere (*Nishida et al.*, 1992). Geotail explored the very distant tail region, having a maximum apogee of 220 R_E and helped to established our understanding of the overall magnetotail geometry.

The Geotail spacecraft was located in the solar wind just upstream of the bow shock during the interval of interest, so we use Geotail as a solar wind monitor. The Magnetic Field Experiment (MGF) (*Kokubun et al.*, 1994) measures the magnetic field vector with a time resolution of 1/16 seconds. The Low Energy Particle experiment (LEP) (*Mukai et al.*, 1994) produces one 3-D distribution function every 12 seconds for ions and electrons in the energy range from several eV to 43 keV.

Chapter 2

Observations

2.1 Overview

This thesis presents a case study of the 25 December 2015 substorm. The THEMIS, ARTEMIS, MMS, and Geotail spacecraft were all aligned approximately parallel to the Earth-Sun line. The distance between Geotail in the solar wind and ARTEMIS P2 in the far-tail is approximately 78 R_E. Table 2.1 provides the position of each spacecraft around the time of substorm onset. Figure 2.1 shows the location of each spacecraft at this time, along with orbit traces for the entire day. Note that the black lines in each panel are magnetic field lines, traced using the Tyganenko 89 model (*Tsyganenko*, 1989). The following sections present data from each mission separately.

Table 2.1: Spacecraft locations at 0815 UT.

Spacecraft	X_{GSM} $[R_E]$	Y_{GSM} $[R_E]$	Z_{GSM} $[R_E]$
ARTEMIS P1	-58.3	-1.0	-5.2
ARTEMIS P2	-61.1	-0.64	-5.0
THEMIS P5	-11.4	2.3	-3.4
THEMIS P3	-11.0	2.3	-4.4
THEMIS P4	-11.1	2.3	-4.0
MMS1[a]	10.8	-2.1	-0.76
GEOTAIL	17.5	5.7	7.8

[a]MMS probes were within a 30 km formation.

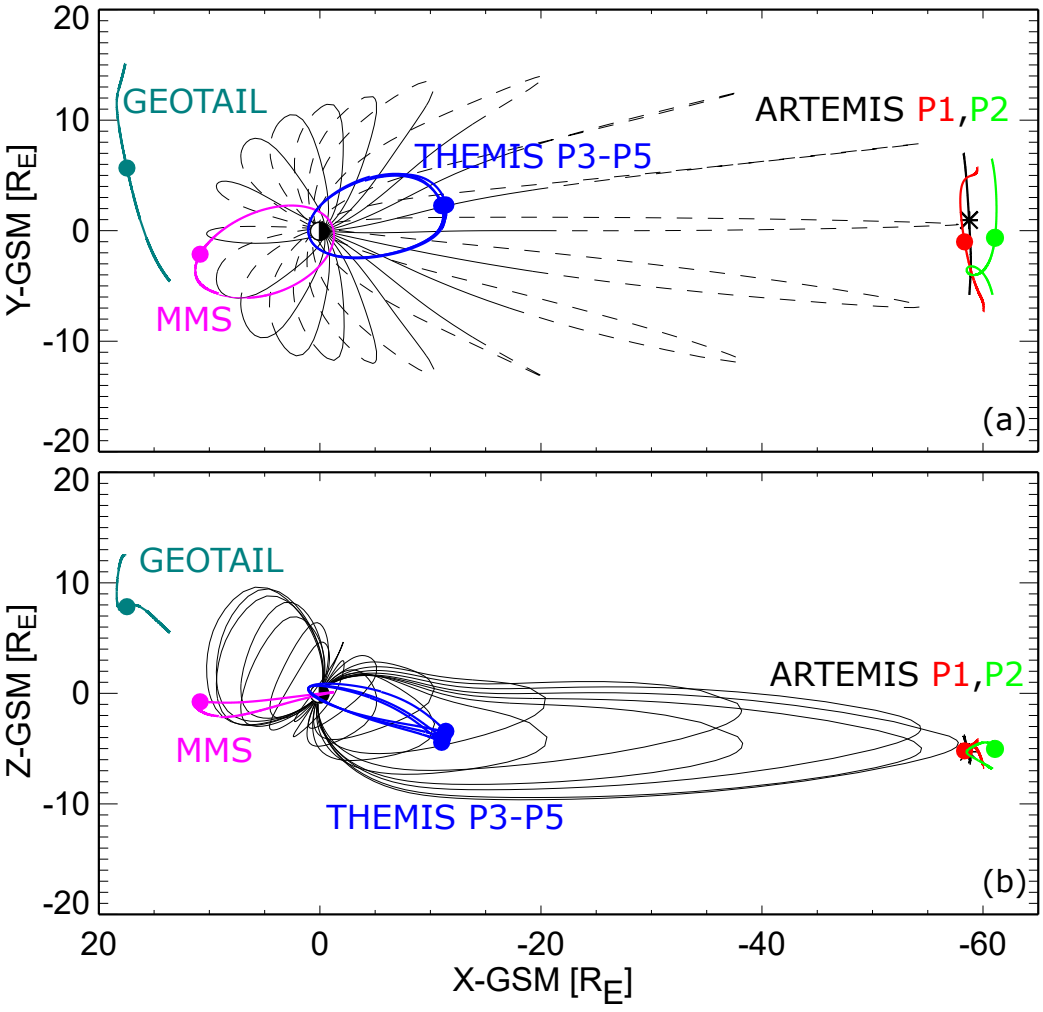

Figure 2.1: Positions of ARTEMIS, THEMIS, MMS, and Geotail spacecraft in the (a) XY plane and (b) XZ plane at 0815 UT on 25 December 2015. The black lines are field lines as traced with the Tsyganenko 89 model. In panel (a), the solid field lines are above the Z = 0 plane, whereas the dashed field lines are below it.

2.2 THEMIS and ARTEMIS Observations

Figure 2.2 shows the magnetic field, particle velocity, and plasma density for the ARTEMIS P1 and P2 and THEMIS P4 probes. This data combines observations from the ESA and SST instruments. The combined data set is produced by performing linear time interpolation to match the timestamps, linear spherical interpolation to match the angular grids, and linear logarithmic energy gap interpolation to fill the energy gap between the instruments.

From 08:17:00 to 08:25:00 UT, the tailward particle velocities (negative V_x) at P1 slowly ramp up from 0 to a maximum value of ∼800 km/sec which persists until 08:33:00. Tailward flow speeds between 500 and 800 km/sec are consistent with reconnection outflow jets reported in case studies of the tail at mid to near-lunar distances (*Øieroset et al.*, 2000; *Oka et al.*, 2011). At 08:19:50, B_x increased from 5 to 10 nT, then began to fluctuate between positive and negative values. At the end of the event interval, B_x turned to -15 nT. P2, which was ∼2.8 R_E further downtail from P1, observed a nearly identical signature, though the particle flows began to increase at 08:19:20 and the magnetic structures arrived at 08:20:10. On the near-Earth side (∼-11.0 R_E), P3-P5 observe a dipolarization front in the magnetic field at 08:17:05, in which the B_x component changes from having a negative value to zero while the B_z component goes from zero to positive (*Runov et al.*, 2011). Only data from P4 is shown, as it is representative of that from the other near-Earth probes. Coincident with the dipolarization front, the earthward flow speed, plasma temperature, and plasma density increase sharply. We interpret these observations as outflows and field signatures associated with reconnection which occurred prior to this time in the mid-tail.

A north-then-south turning of the magnetic field, as was observed by P1 and P2, is generally accepted as a signature of a passing plasmoid in the tail. To confirm that the observed structure is indeed a plasmoid, the pressure enhancement inside the plasmoid should be at least 10% of the baseline value, as discussed by *Ieda et al.* (1998). The pressure instead the structure has a

maximum near >0.09 nPa, whereas the baseline value before the event was ∼0.065 nPa, indicating a total pressure enhancement of ∼38%. Therefore, we conclude that this structure is indeed a passing plasmoid ejected tailward during the reconnection. The observed plasmoid matches typical parameters determined in statistical studies of plasmoids using Geotail observations. The ion temperature inside the structure of between 3 and 5 keV is similar to that reported by *Ieda et al.* (1998), as is the ion to electron temperature ratio of ∼16.

P2 was 2.8 R_E further downtail from P1 and observed the same particle flows 111 sec after P1. This time delay indicates that the plasmoid structure was moving at a velocity of ∼160 km/sec tailward. Assuming the plasmoid is neither accelerating nor expanding, the overall length can be estimated by considering the duration over which the flow channel was observed. Considering that the flows persisted for 16 minutes, this gives an estimate for the plasmoid length as ∼20 R_E. *Nagai et al.* (1997) reported a median flow duration for plasmoids between -100 and -80 R_E to be 17 minutes, comparable to the expansion phase of substorms. Previous estimates for plasmoid length have ranged from 17 to 35 R_E (*Slavin et al.*, 1984; *Moldwin and Hughes*, 1992).

It is important to note that even though the observed ion bulk plasma velocities are > 500 km/sec tailward, the estimated plasmoid velocity is only about 200 km/sec tailward once it has reached lunar distances. It is possible that the plasmoid is expanding or accelerating, though one cannot determine this from two-point measurements.

Figure 2.3 (left) shows the ion pitch angle distribution for particles measured by both the ESA and SST instruments. Values are interpolated for the energy bands which fall in the gap between the two instrument measurement ranges. From 08:20 UT to 08:28 UT, the pitch angles are primarily in the anti-parallel direction. For positive (earthward) B_x during this time, this indicates these particles were traveling tailward and away from the re-

connection site, as expected. In between 08:28 UT and 08:33 UT, the pitch angle alternates between values near 0 and 180°. This occurs because B_x is alternating from positive to negative values. The highlighted regions in the figure show that the pitch angles during intervals of positive B_x are antiparallel and the pitch angles during intervals of negative B_x are parallel. Thus, the particles continue flowing in the tailward direction throughout the entire observation interval. We interpret the fluctuations in B_x as a flapping mode of the current sheet, as B_x will be positive (earthward) above the midplane and negative (tailward) below it. Figure 2.4 shows a diagram of the magnetotail for each of these cases. For the few quasi-periodic oscillations which are observed, the average period is ∼65 sec so the frequency of this flapping motion is estimated to be ∼0.015 Hz. These values are consistent with previous studies of current sheet flapping associated with fast flows or geomagnetic activity (e.g., *Sergeev et al.*, 2003, 1998; *Runov et al.*, 2009b).

The black lines in the lower panel of Figure 2.3 denote the limiting pitch angle for particles trapped inside the flow channel structure. The field within the flow channel is weaker in magnitude than that outside, thus creating a magnetic bottle configuration. We use the method described in *Nykyri et al.* (2012) to determine the limiting pitch angle, α, which depends only on the field inside the flow channel, B_2 (time varying), and the maximum absolute value of the field outside the flow channel, B_1 (assumed to be constant 15 nT). The expression for the limiting pitch angle is as follows:

$$\alpha = asin\left(\sqrt{\frac{B_2}{B_1}}\right). \tag{2.1}$$

The particles in between the limiting pitch angle curves are trapped inside the flow channel and must have originated from nearer to the reconnection site, traveling to the observation site inside the plasmoid.

Figure 2.5 shows a schematic of the magnetic field geometry relative to the spacecraft trajectory. For the interval from 08:00 to 09:00, the magnetic field

data from P1 was downsampled to a cadence of 12 seconds and then plotted as vectors in the XZ plane along the spacecraft trajectory. An example field configuration has been superimposed to illustrate how the magnetic field observed by P1 agrees with the classic tail geometry associated with reconnection.

The oppositely directed flows at P1-P2 and P3-P5 indicate that the reconnection X-line was located in the mid-tail region between these observation points. Given the positions of two probes on either side of the reconnection location and the times at which substorm phenomena was first detected at each location, we can determine the time and location at which reconnection occurred. Unlike previous work which assumes a constant propagation speed on both sides of the reconnection site (*Angelopoulos et al.*, 2008; *Liu et al.*, 2009; *Mende et al.*, 2009b), we use here the equations presented by *Liu et al.* (2011) which allow for different tailward and Earthward propagation speeds. Whereas assuming a constant propagation speed is reasonable over short distances, this assumption is invalid considering the >45 R_E probe separation considered in this event. We do assume that the propagation speed is constant on either side of the reconnection site and that the propagation is entirely in the X-direction. These equations are as follows:

$$X_E - X_R = V_E \left(T_E - T_R\right), \tag{2.2}$$

$$X_R - X_T = V_T \left(T_T - T_R\right), \tag{2.3}$$

where X_R and T_R are the location and time of the reconnection site, respectively, V_E and V_T are the Earthward and tailward magnetosonic speeds, X_E and X_T are the respective probe positions, and T_E and T_T are the times at which the signatures were observed in each location. The inferred reconnection position and onset time are heavily dependent on the magnetosonic speeds used in the calculation. Figure 2.6 shows the reconnection site and

time with varying earthward and tailward magnetosonic speeds. We consider the dipolarization field at P3 (08:17:05) as the earthward observation time and the magnetic structure at P1 as the tailward observation time (08:19:50). Assuming an earthward propagation speed of 800-1000 km/sec and a tailward propagation speed of 400-600 km/sec, the reconnection site is determined to be 33.2 $\pm$ 2.4 R_E. The reconnection onset time for this range is 08:13:49 - 08:14:59.

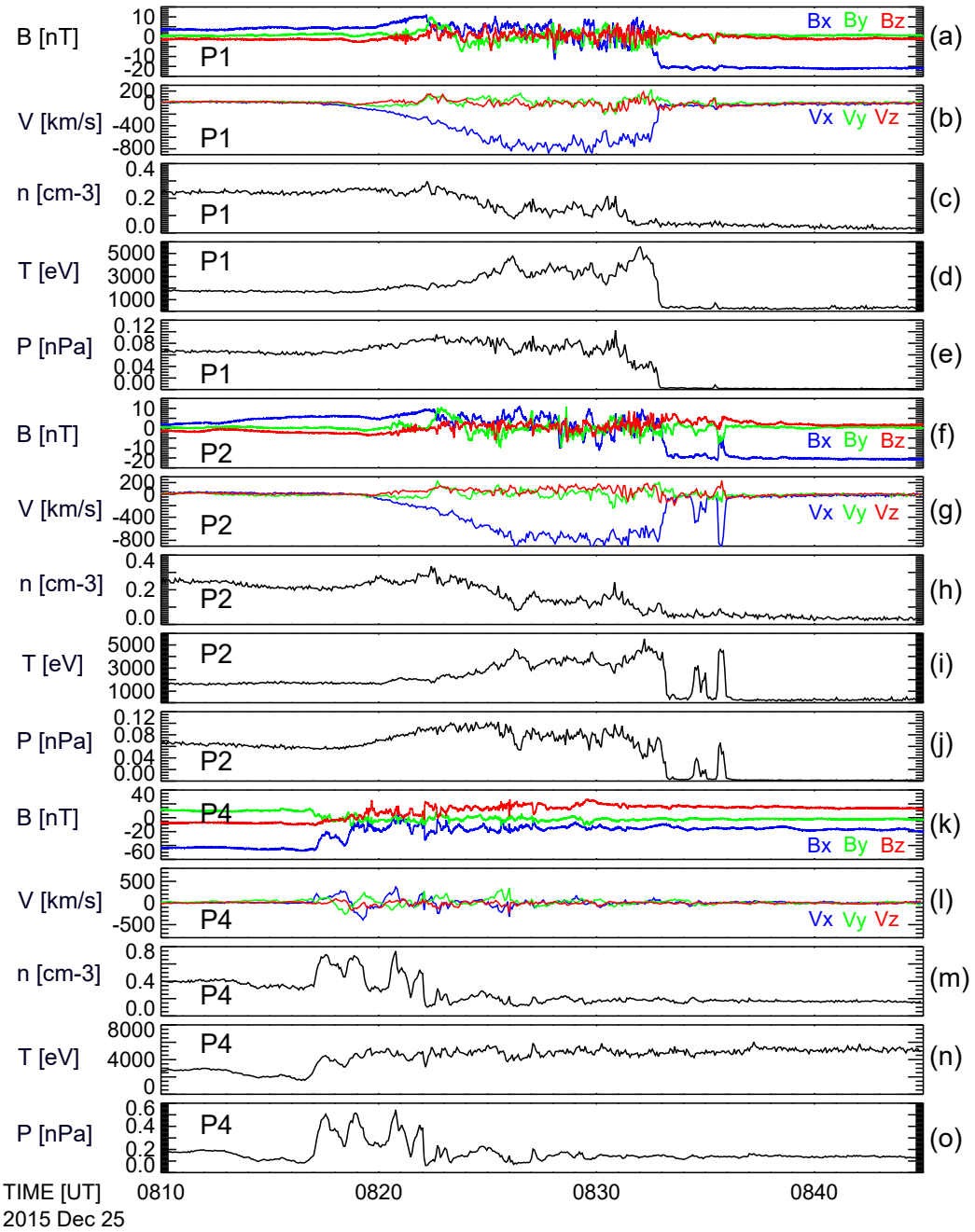

Figure 2.2: Magnetic field, ion bulk velocity, density, temperature, and pressure for ARTEMIS (a-e) P1 and (f-j) P2 and (k-o) THEMIS P4.

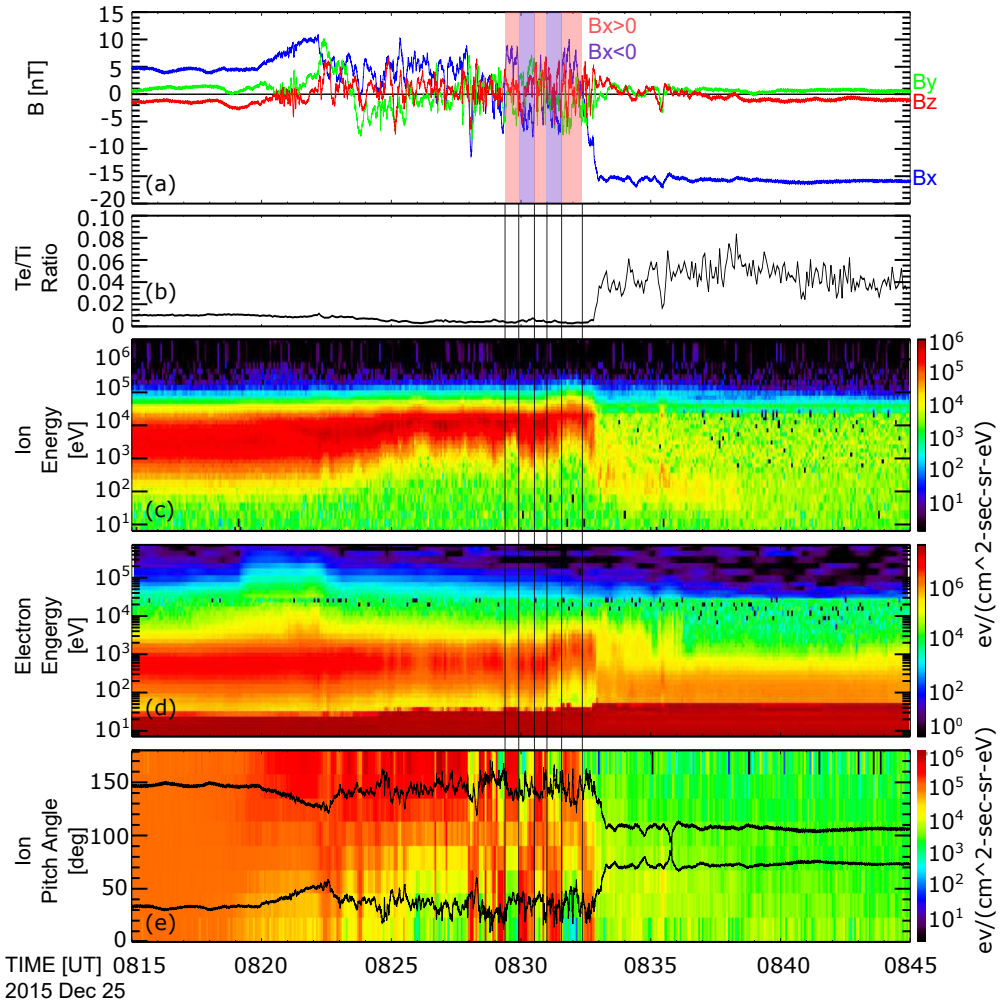

Figure 2.3: (a) Magnetic field, (b) electron to ion temperature ratio, (c, d) ion and electron energies, and (e) ion pitch angle distribution data from ARTEMIS P1. The light red boxes in (a) indicate where B_x was positive and the light blue boxes indicate where B_x was negative. The vertical lines through panels (b-e) indicate the times where B_x was zero. The periodic variations of the ion pitch angles match the variations of B_x. The black line in panel (e) shows the limiting pitch angle for particles inside the flow channel.

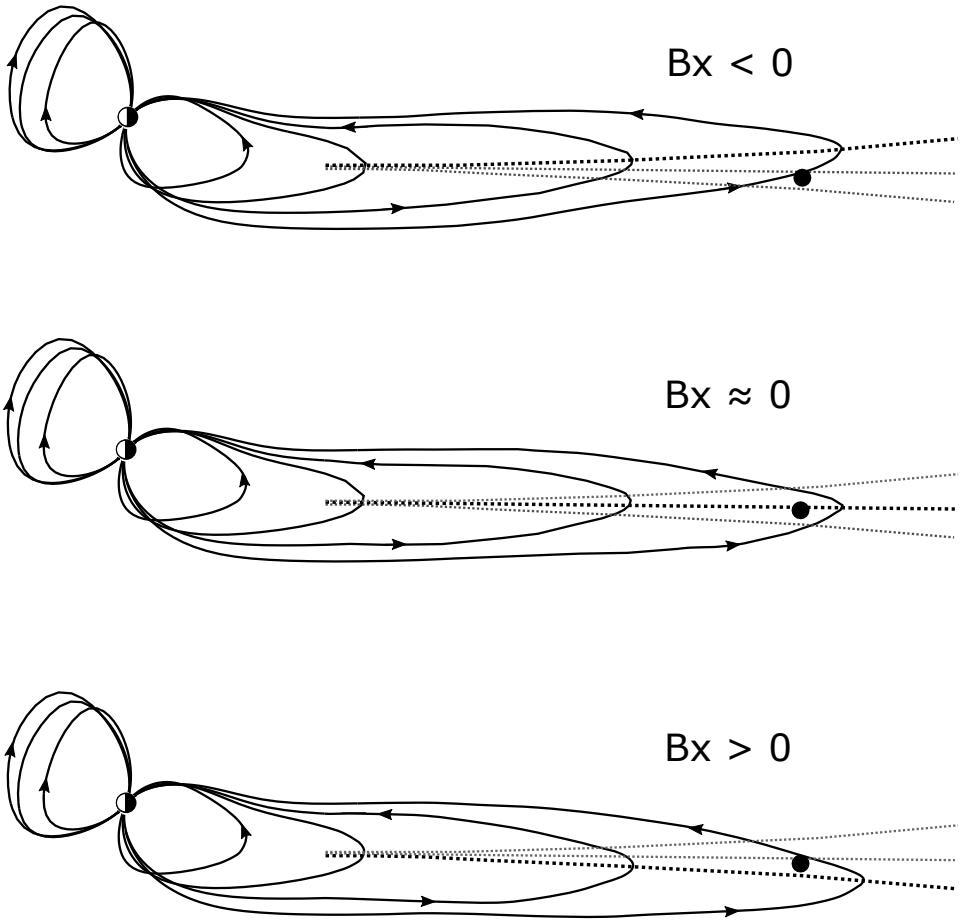

Figure 2.4: Schematic depicting a flapping motion of the current sheet in the tail. As the current sheet moves above or below the spacecraft (black dot), the measured B_x component of the magnetic field will change. The spacecraft is in the same location relative to Earth in each panel. The black dotted lines in each panel show the current sheet and the grey dotted lines show the current sheet shape in the other cases.

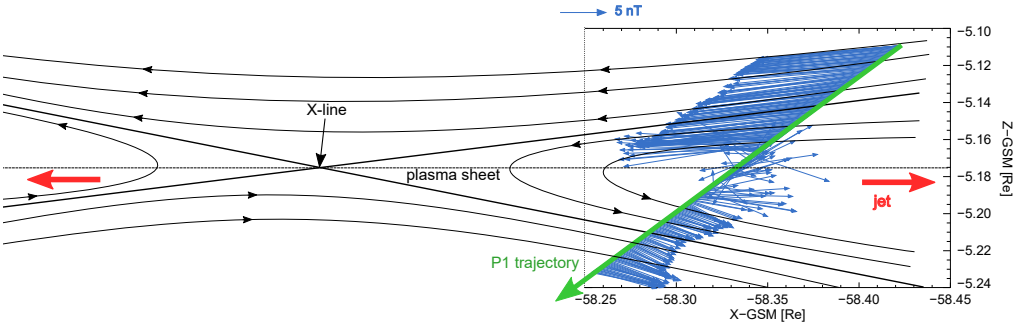

Figure 2.5: Schematic showing the magnetic field vectors plotted along the trajectory of ARTEMIS P1 in between 08:00 and 09:00 The black lines show a possible magnetic field configuration which matches the observed field.

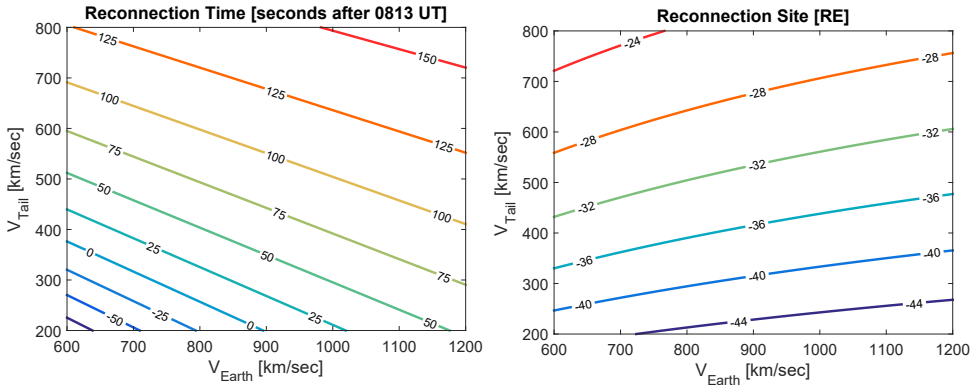

Figure 2.6: (left) Reconnection onset time and (right) X-line location dependence on propagation speeds.

2.3 Ground Observations

During the substorm event on 25 December 2015, the ground-based magnetometer stations and all-sky imager observatories captured magnetic signatures and auroral intensification related to the magnetotail phenomena. Figure 2.8 shows data from the stations at Poker Flat, AK (POKR), Inuvik, NT (INUV), Whitehorse, YT (WHIT), Petersburg, AK (PTRS), Fort Simpson, NT (FSIM), Fort Smith, NT (FSMI), Gillam, MB (GILL). In addition, the auroral electrojet (AE) index derived from the THEMIS magnetometer network is shown along with total intensity counts from the FSMI ASI. The location of each station and the ionospheric footprints of P3-P5 (traced using the Tsyganenko 89 model) are shown in Figure 2.7. Table 2.2 provides the location of each station. Note that P1 and P2 were located at field lines which do not map to the Earth. At each of the stations, magnetic pulsations in the Pi2 range (40-150 sec) (*Saito*, 1969) associated with a substorm current wedge (SCW) are detected beginning at 08:17:33 (denoted by the dashed vertical line). Further, the AE index first decreases slightly then increases to ∼450 nT and the auroral intensity captured by the FMSI ASI increases sharply at this time. This is in agreement with the previously determined reconnection time, considering a typical time delay between reconnection and ground onset of 2-4 minutes.

At FSIM and all stations eastward (FILL, FSMI), the initial turning of the

Table 2.2: Locations of ground stations arranged from west to east.

Station	Mag. Lat. [$^{\circ}N$]	Mag. Lon. [$^{\circ}W$]
POKR	65.40	265.79
INUV	71.21	275.77
WHIT	63.64	279.62
PTRS	59.90	283.97
FSIM	67.23	294.41
FSMI	67.29	307.05
GILL	66.00	333.19

D (East) component is negative, whereas for PTRS and all stations westward (WHIT, INUV, POKR), the initial turning is positive. This indicates that the center of the SCW is located between FSIM and PTRS, corresponding closely to the THEMIS footprints and a magnetic local time of 23.00.

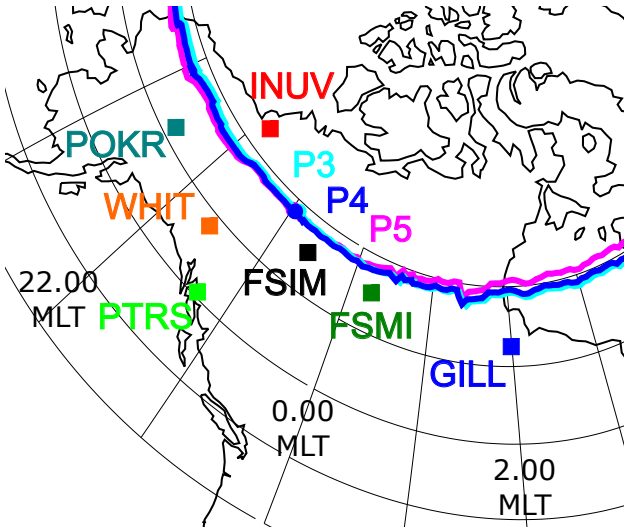

Figure 2.7: Locations of the ground-based observatories and footprints of the THEMIS probes at 08:17:00 traced using the Tsyganenko 89 model.

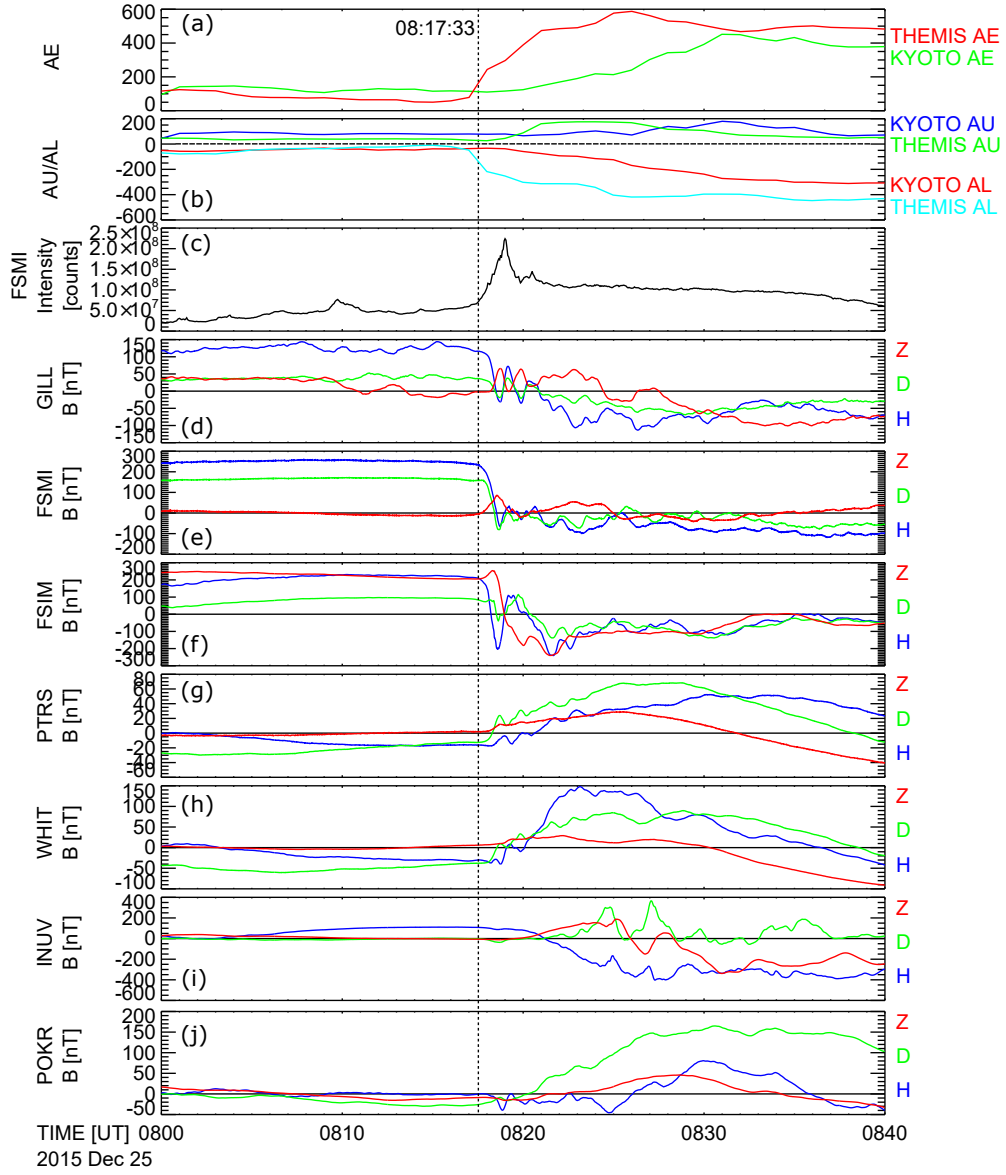

Figure 2.8: AE (a), AU and AL (b) indices, total all-sky imager intensity at FSMI (c), and ground based magnetometer data from stations arranged from east to west (d)-(j). The dashed vertical line indicates 08:17:33, the ground onset time of the substorm.

2.4 Solar Wind Observations

The Geotail spacecraft was located in the solar wind during the event interval, just outside of the bow shock. Therefore, the plasma parameters and magnetic field observed by Geotail, shown in Figure 2.9, are indicative of those acting upon the magnetosphere. In addition, field and plasma parameters from the OMNI virtual spacecraft and ACE (propagated to the bow shock nose) are provided and are in good agreement with the Geotail observations. Geotail observes a large-scale oscillation of the IMF from 07:00 to 09:00 on 25 December 2015. Figure 2.10 shows this large-scale structure plotted as vectors along the line directly upstream from Geotail. The panels showing the structure are aligned with the Geotail spacecraft to create a quasi-scale visualization of the IMF. Each vector is shifted upstream a distance equal to $v_x t$, where v_x is the average solar wind speed in the X-direction (-540 km/sec) and t is the time in seconds past 07:00.

It is generally accepted that anti-parallel components are required for reconnection to occur at the dayside magnetopause, which occurs most effectively for strong southward IMF. This allows magnetic flux to accumulate in the tail, eventually leading to a global substorm. Assuming the magnetic field lines propagate earthward in the dayside magnetosheath with a typical speed of 100 km/sec (consistent with that observed near the magnetopause) and from the dawn-dusk terminator tailward with a typical speed of 550 km/sec (equivalent to the mean solar wind speed), a B_z component associated with dayside reconnection would be expected at the Geotail location 17-18 minutes prior to the tail reconnection, or around 07:56. However, the magnetic field observed by Geotail shows that B_z is positive after 07:52 and has negative values very near to zero ($\sim$-2 nT) from 07:40 to 07:52 UT. This is clearly denoted by the vertical line in Figure 2.10. Thus, the expected strong negative B_z signature is not present.

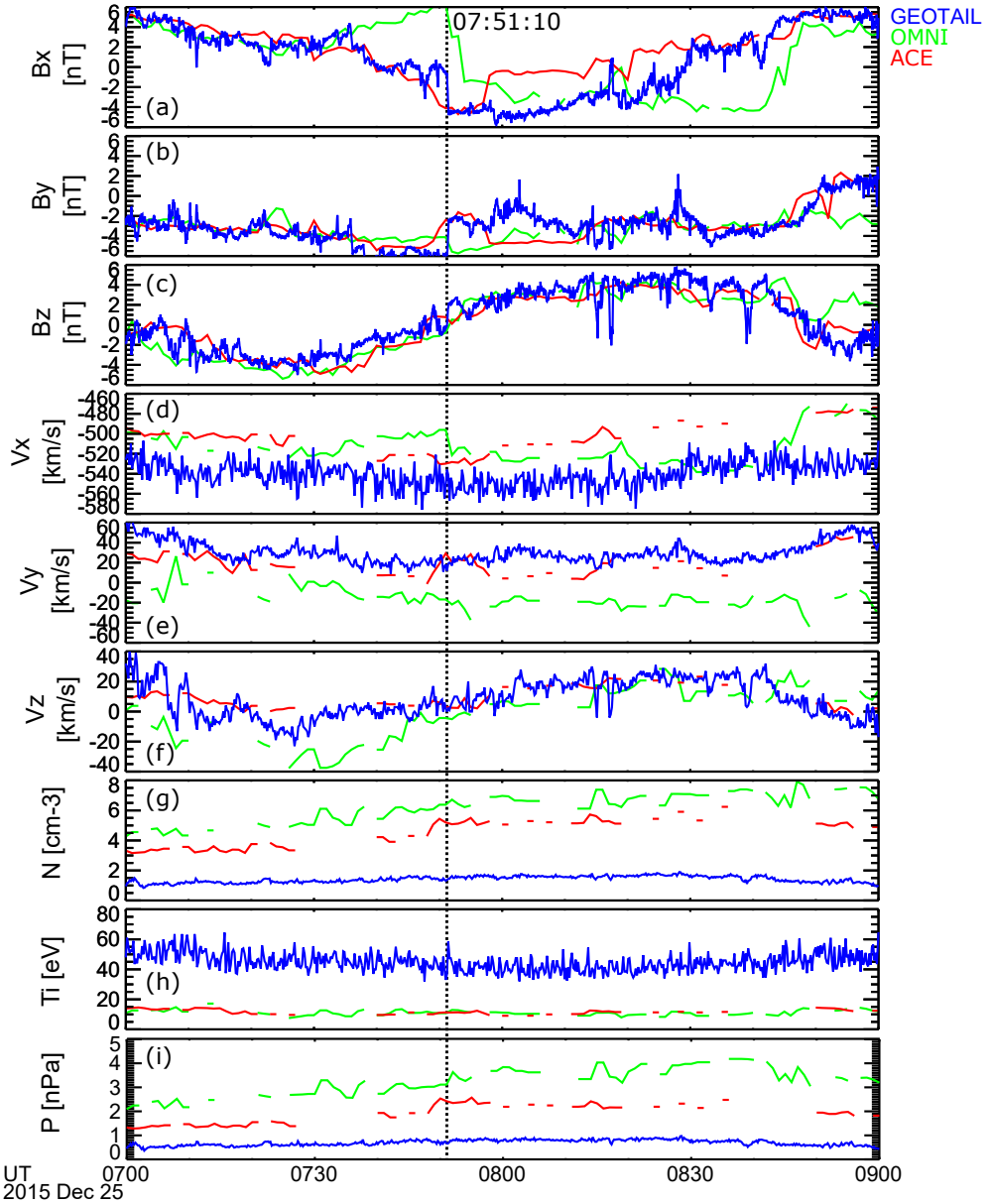

Figure 2.9: Magnetic field components (a)-(c), velocity components (d)-(f), ion density (g), and ion temperature (h) in the solar wind prior to the substorm observed by Geotail, ACE (propagated to bow shock), and OMNI.

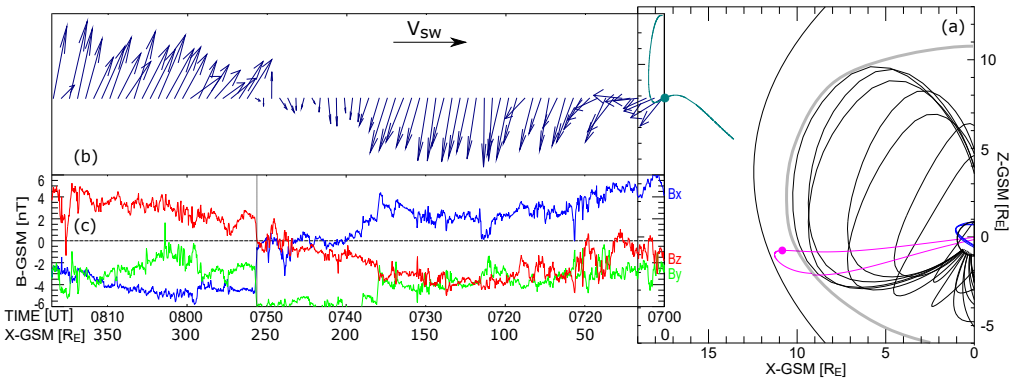

Figure 2.10: Schematic of the structure observed in the solar wind by Geotail, ACE, and OMNI. Panel (a) shows a detail view of the dayside magnetosphere (XZ plane) with the locations of Geotail and MMS. Panel (b) shows the solar wind magnetic structure observed by Geotail plotted as vectors along the direct, upstream line. The vectors are derived from Geotail data downsampled to 1 minute resolution. Assuming a constant propagation speed of 540 km/sec, the entire structure would propagate to the right and the last vector would reach the Geotail location at 08:17 UT. Panel (c) shows the actual magnetic field components from which the vectors were derived. The vertical line denotes 07:51:50, the time at which B_z becomes positive (northward).

2.5 MMS Observations

During the 25 December 2015 substorm, the MMS spacecraft were located in the dayside magnetosheath, just outside the magnetopause boundary (see Figure 2.1 and Table 2.1). In the minutes prior to the substorm onset in the tail, MMS detected very large fluctuations in the magnetic field. Figure 2.11 shows magnetic field and plasma data for MMS from 07:50 to 08:30. The very strong southward magnetic field ($B_z \approx$ -25 nT) associated with the pulses at 08:00:20 and 08:06:00 could have initiated the reconnection on the dayside. Assuming a propagation speed of 200 km/sec from the MMS location to the dawn-dusk terminator and a propagation speed of 550 km/sec (close to the average solar wind speed during this interval) from the terminator to the reconnection site, the resultant time delay from the MMS location to the reconnection site is 12 minutes. This indicates that magnetic field lines opened by the strong southward field observed by MMS would have propagated tailward and arrived at the mid-tail reconnection site very close to the previously inferred time of ∼08:14, potentially triggering the substorm. We propose several possibilities regarding the fluctuations observed by MMS. (1) It is feasible that the pulse is a smaller-scale structure in the solar wind which was not detected by the upstream monitors. When passing through the bow shock, the magnitudes increased by a typical shock compression factor of ∼4, thus explaining the large amplitudes. (2) The pulse could have formed as a result of a kinetic shock process due to a discontinuity in the solar wind hitting the bow shock. (3) This is a structure in the magnetopause boundary, possibly an FTE, through which MMS momentarily passed. These possibilities will be discussed further in Section 4.

In the minutes prior to 08:00, MMS observed large fluctuations in the magnetic field magnitude which were anticorrelated with fluctuations in the plasma pressure. These characteristics are indicative of a mirror mode instability (*Hasegawa*, 1969; *Tsurutani et al.*, 1982). Mirror structures are non-propagating and predominantly occur in regions where the plasma $\beta >$

5, which is the case for this interval (β is the ratio of the plasma pressure $p = nkT$ to the magnetic pressure $p_B = B^2/2\mu_0$). The presence of a mirror mode instability in close proximity to the possible dayside reconnection site is significant because mirror mode structures could be a form of wave activity which creates anomalous resistivity required for reconnection, as discussed by *Treumann et al.* (2004). A more in-depth analysis of the MMS observations for the 25 December 2015 substorm is left for future studies.

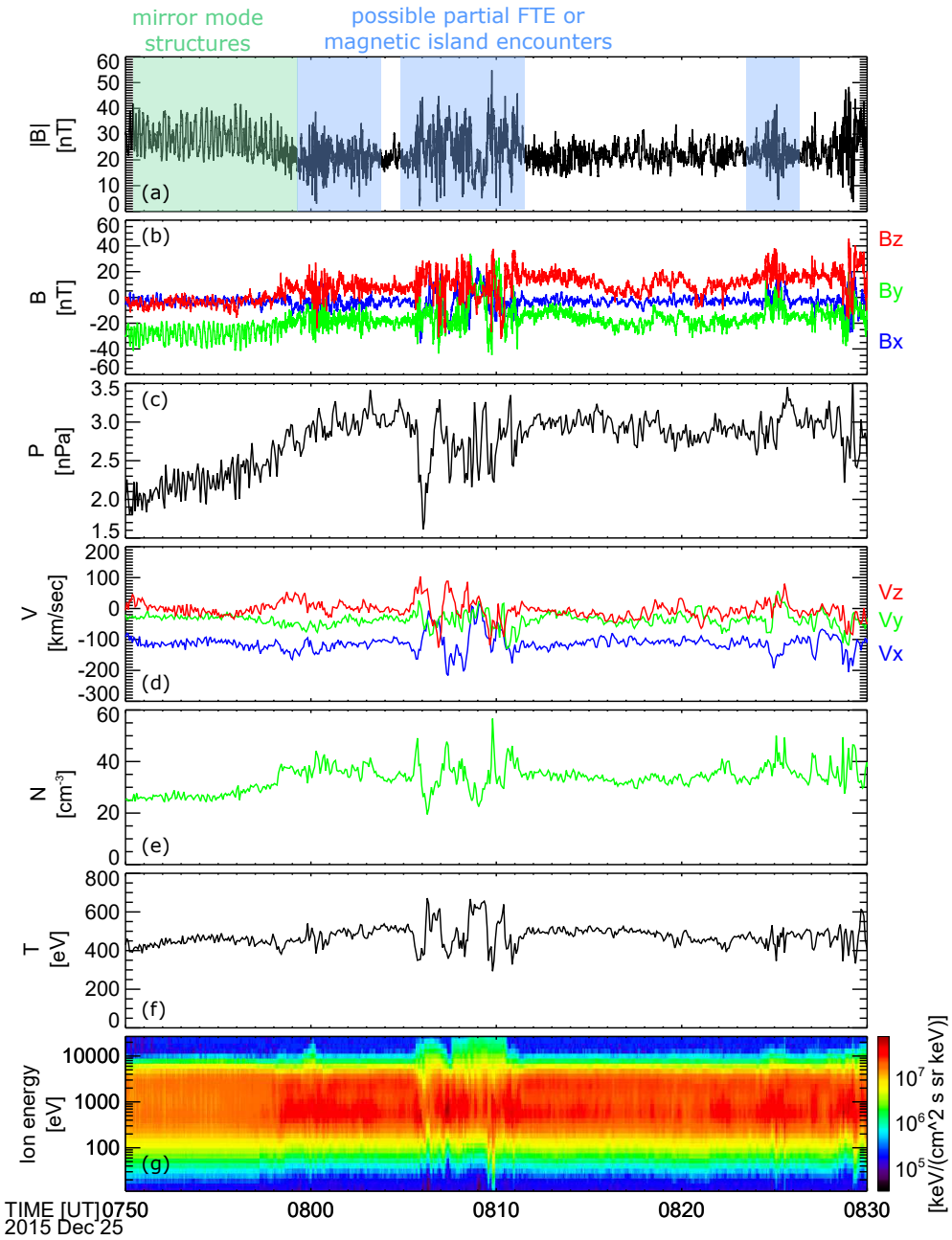

Figure 2.11: Magnetic field and plasma parameters in the magnetosheath observed by MMS1. Total magnetic field (a), magnetic field vectors (b), pressure (c), bulk velocity (d), density (e), temperature (f), and energy distribution for ions (g). The green highlighted region is where mirror mode structures were observed. The blue boxes denote times where FTE structures may have been encountered.

Chapter 3

Simulations

The global magnetosphere was modeled for the 25 December 2015 substorm using the Block-Adaptive-Tree-Solarwind-Upwind-Roe-Scheme (BATS-R-US) model integrated into the Space Weather Modeling Framework (SWMF) hosted by NASA's Community Coordinated Modeling Center (CCMC). The model was developed by the Center for Space Environment Modeling at the University of Michigan. The code was written in Fortran 90 and runs on a highly parallelized computer cluster. BATS-R-US solves the 3-D MHD equations using the finite volume method and a solver derived from Roe's approximate Riemann solver. An advantage of this code is that it uses an adaptive grid with varying spatial resolutions.

A custom, high-resolution grid was generated with the region bounded by $-70 < x < 16, |y| < 24, |z| < 12$ (all dimensions in R_E) resolved with a 1/4 R_E grid. A finer grid of 1/8 R_E resolution was added to the likely reconnection site locations: $-48 < x < 0, |y| < 24, |z| < 12$ and a sphere around the Earth with a radius of 16 R_E. The computational grid has a 1 R_E resolution for areas outside those described above. In total, the grid has 9,623,552 cells. Figure 3.1 shows the computational grid used in the simulation. The code time resolution is 1 minute.

Geotail was located in the pristine solar wind just upstream of the bow

shock, so the actual Geotail data (shown in Figure 2.9 was used as an input to the model. The model generally does not perform well for varying B_x and inputs with constant value or single step change are highly recommended by the CCMC personnel. Therefore, B_x was chosen to be 2 nT until 07:48:30 and -4 nT for the remainder of the run. This is consistent with the discontinuity in B_x present at this time in the actual data. Note that the Geotail input data was propagated upstream to the model boundary at 33 R_E.

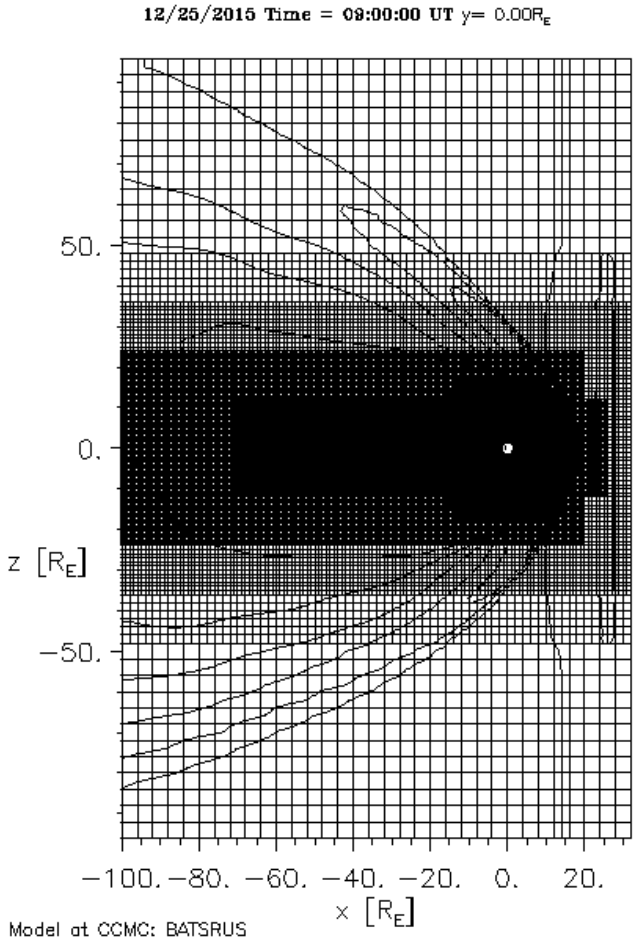

Figure 3.1: Computational grid used in the BATS-R-US model of the 25 December 2015 substorm.

The simulation results are shown in Figures 3.2, 3.3, and 3.4. Strong earthward and tailward jets consistent with reconnection are visible as early as 07:40, indicating that the model produced reconnection somewhat earlier than the observations show. The X-line location remains between -55 and -50 R_E until 08:30, at which time it retreats beyond the simulation domain. The flows steadily increase from 07:40 to 08:00, reaching a maximum magnitude at 08:00 of approximately 1250 km/sec earthward and 1000 km/sec tailward. A plasmoid is ejected from the reconnection site tailward at 07:45.

Figure 3.5 shows a comparison between data from THEMIS P3 and a virtual THEMIS P3 in the simulation. In the simulation results, the virtual P3 probe observes outflow jets with a maximum velocity near 600 km/sec and magnetic field structures, both of which correlate very well with the observations. The outflow observed by THEMIS P3 from 07:50 to 08:00 is not detected by THEMIS P4 or P5, which were separated by less than 0.3 R_E in X, less than 1 R_E in Z, and shared the same Y coordinate. This indicates that the flow channel was spatially localized, corresponding to a bursty bulk flow (BBF) rather than a dipolarization front. BBFs are caused by spatially and temporally localized reconnection events and are the dominant mechanism for earthward mass, energy, and flux transfer in the midtail (*Angelopoulos et al.*, 1994; *Wiltberger et al.*, 2015). The model produces these signatures 14 minutes earlier than they actually occurred, so the virtual probe data in Figure 3.5 has been shifted by 14 minutes. Once time-shifted, the simulation and observations agree very closely for both the BBF from 07:50 to 08:00 and the dipolarization signatures at 08:17.

Though the BBF event indicates reconnection activity before 08:00, this does not suggest a substorm onset time earlier than previously determined. A number of other factors have been used to determine the later onset time of approximately 08:14 which are not present at this earlier time. The ARTEMIS field and plasma observations do not indicate a tailward moving plasmoid around 08:00. There are no Pi2 pulsations detected on the ground

and there is minimal auroral activity at this time. Further, after the flows from 07:50 to 08:00, the magnetic field strength remains large (B_x = -45 nT) until the dipolarization at 08:17. These factors indicate that the signature observed by THEMIS P3 between 07:50 and 08:00 is indeed a localized BBF, rather than a global field reconfiguration consistent with a substorm. During the BBF, some of the flux accumulated in the tail during the long interval of solar wind driving from 07:15 to 07:40 was released into particle kinetic and thermal energy, though the energy transfer was not significant enough to trigger a substorm. As a result, the global magnetosphere remained in a marginally unstable state in which a large amount of energy was stored in the magnetotail. The weakening solar wind coupling after from 07:40 did not provide a sufficient trigger to cause substorm onset.

BATS-R-US is an ideal MHD code which does not include a model for the small-scale physics associated with magnetic reconnection. Numerical diffusion associated with the discretized simulation grid manifests itself as increased resistivity in the plasma. Such resistivity is what violates the frozen-in condition and allows reconnection to occur. One interpretation of the numerical resistivity is that two magnetic field lines can reconnect if they meet in the same grid cell. Though a special, high-resolution grid was used in the areas where reconnection is likely to occur, the grid sizes remain much larger than the typical scale sizes of reconnection regions. One likely reason for the 14 minute time discrepancy in the simulation results is that the physical processes which cause reconnection take place over some time, whereas the simulation field lines can reconnect more readily and over a wider region because of the numerical resistivity, resulting in higher reconnection rate. Overall, the effects of numerical resistivity for this specific simulation have not been comprehensively analyzed.

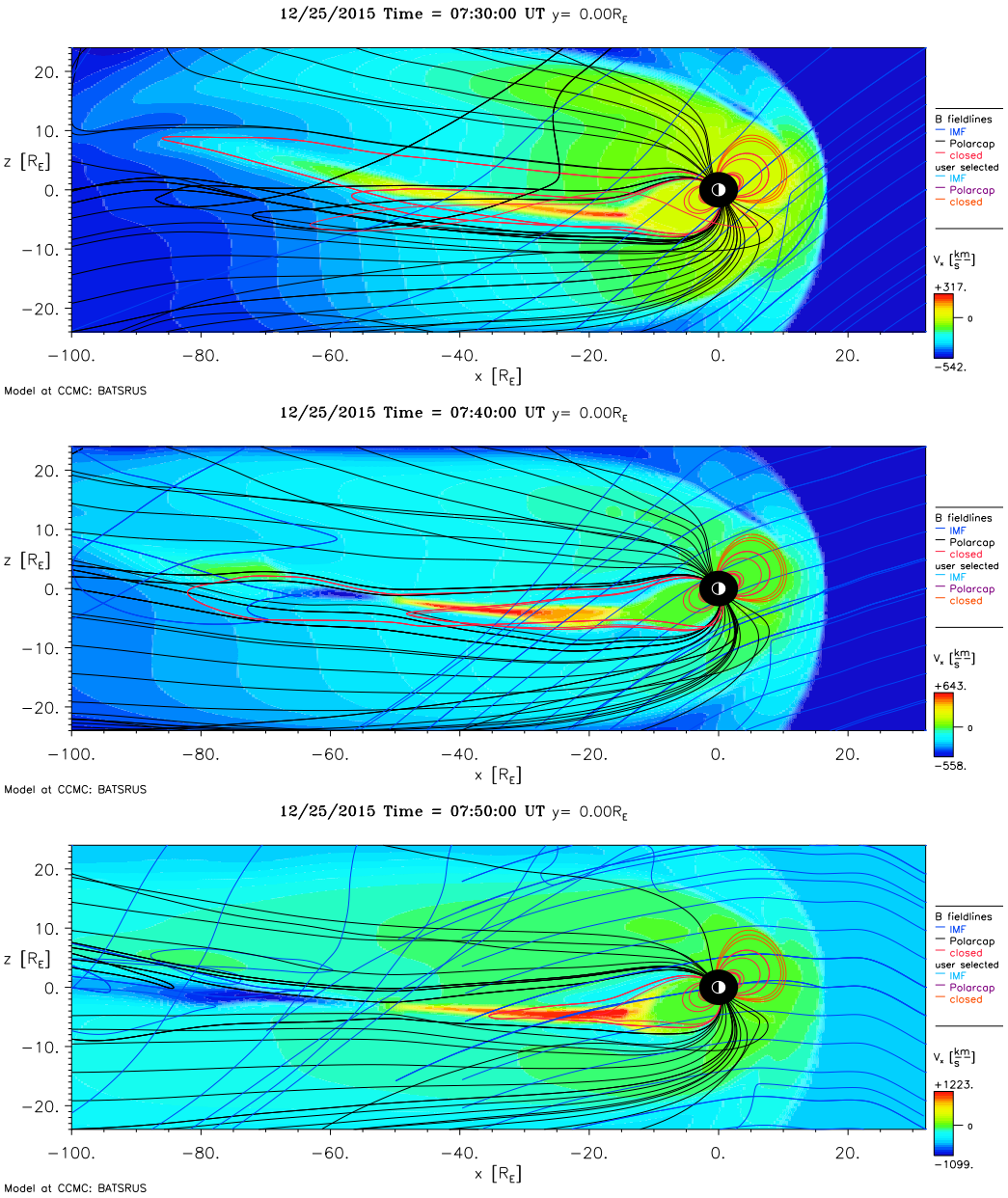

Figure 3.2: X-Z plane view of the global magnetosphere simulation results at 07:30 (upper), 07:40 (center), and 07:50 (lower). The black lines indicate open magnetic field lines, red lines indicate closed, and blue lines are the IMF. The color indicates the flow speed in the X-GSM direction. Red regions indicate earthward flow and blue regions indicate tailward flow.

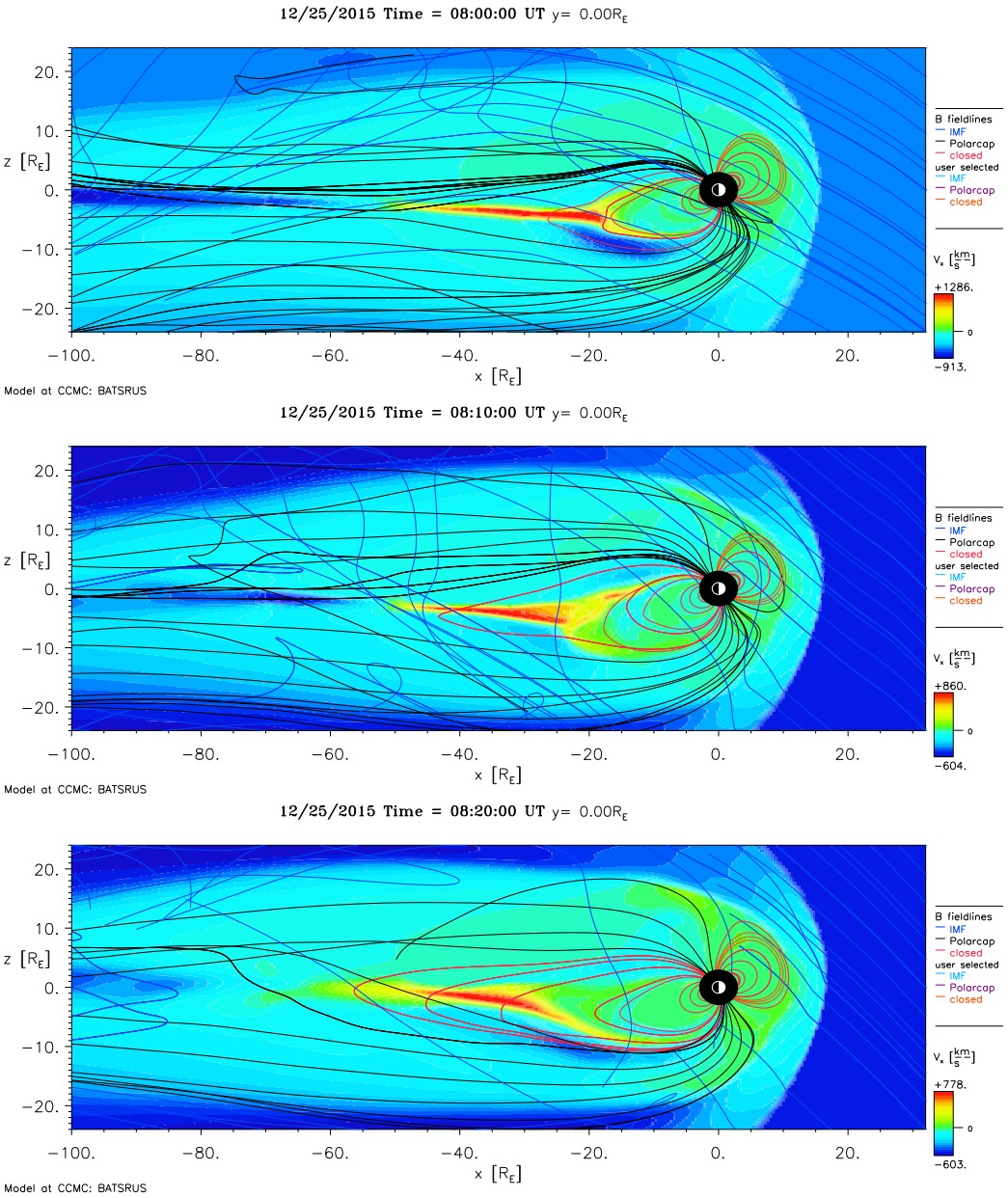

Figure 3.3: X-Z plane view of the global magnetosphere simulation results at 08:00 (upper), 08:10 (center), and 08:20 (lower). The black lines indicate open magnetic field lines, red lines indicate closed, and blue lines are the IMF. The color indicates the flow speed in the X-GSM direction. Red regions indicate earthward flow and blue regions indicate tailward flow.

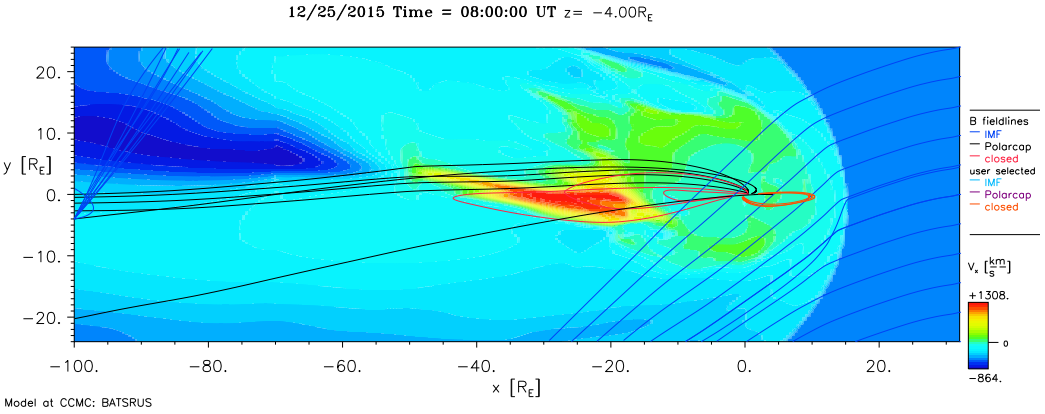

Figure 3.4: X-Y plane view of the global magnetosphere simulation results at 08:00. The black lines indicate open magnetic field lines, red lines indicate closed, and blue lines are the IMF. The color indicates the flow speed in the X-GSM direction. Red regions indicate earthward flow and blue regions indicate tailward flow.

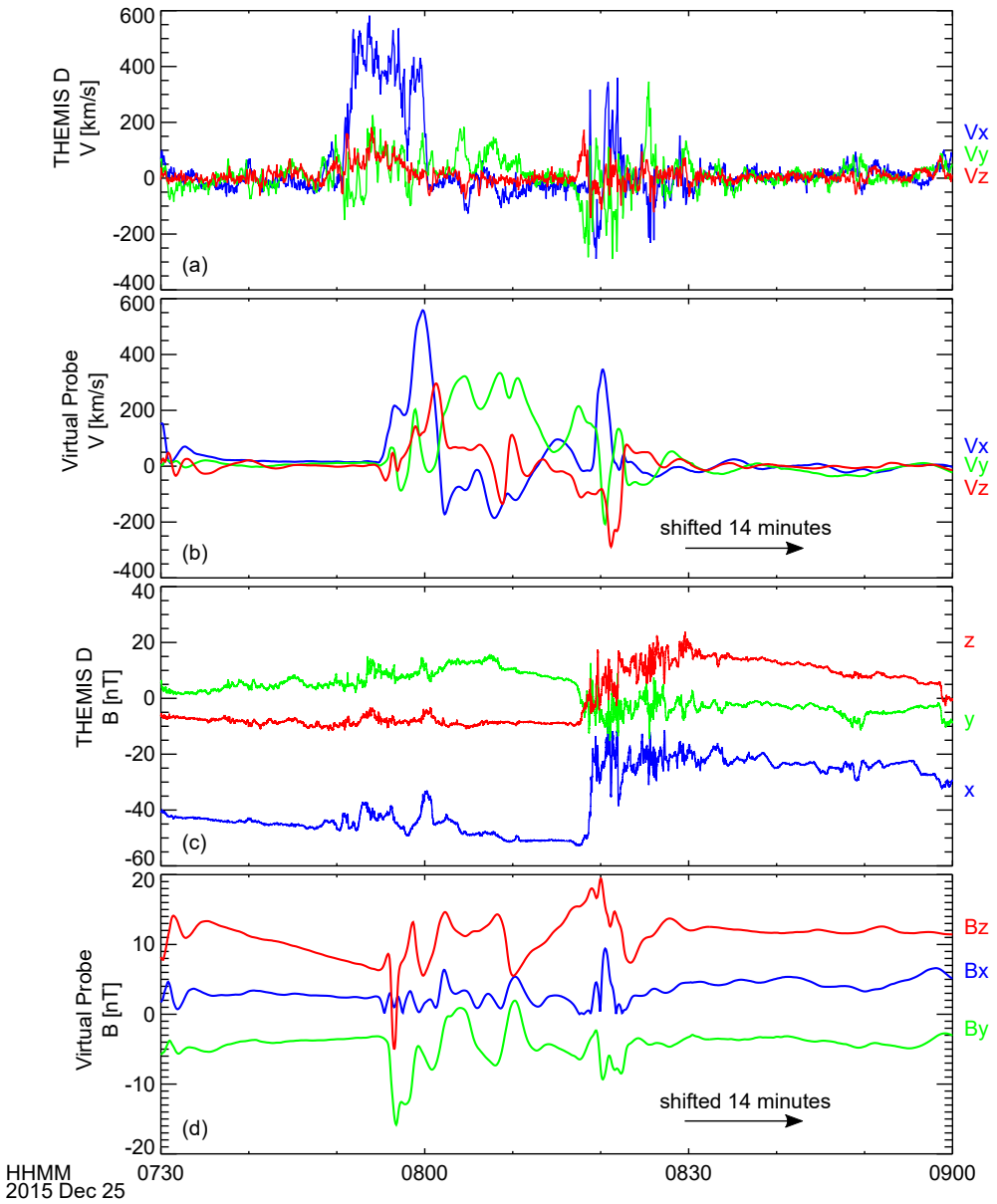

Figure 3.5: THEMIS P3 actual and virtual probe plasma velocity (a, b) and magnetic field (c, d) data. The virtual probe data has been time-shifted by 14 minutes to more clearly show the agreement between the model and observations.

Chapter 4

Discussion

4.0.1 Timing Analysis and Substorm Trigger

Many recent studies have utilized the multipoint THEMIS data to construct a time history of substorm events in the tail. This process is followed in this thesis by applying timing analysis to the THEMIS and ARTEMIS data sets. Assuming different tailward and earthward propagation speeds, the reconnection location and time are determined to be 33.2 $\pm$ 2.4 R_E and 08:13:49 - 08:14:59. This result gives propagation delays to the observation sites and ground consistent with previously reported values. This work, however, builds upon previous studies by applying timing methods to the entire magnetospheric system, rather than only considering the tail. The fortuitous near-alignment of several spacecraft missions along the Earth-Sun line during the Christmas Day 2015 substorm allows us to extend the method to the global scale, constructing a time history all the way from the solar wind during the growth phase to the energy dissipation of the expansion phase. Table 4.1 shows a time history of the global magnetosphere for the events leading up to the substorm onset.

The propagation speed of opened field lines from the dayside magnetopause to the tail is not constant. Rather, the lines travel more slowly until

Table 4.1: Timeline of events during the Christmas Day 2015 substorm.

Time [UT]	Location	Instrument	Event
07:52:00	solar wind	Geotail	IMF turns northward
08:01:00	magnetosheath	MMS	magnetic fluctuations
08:14:00	X_{GSM} = -33.2 R_E	-	inferred tail reconnection
08:17:05	far tail	P1	tailward flows increase
08:17:05	near tail	P3-P5	dipolarization signature
08:17:33	ground	GBOs	Pi2 pulsations
08:19:20	far tail	P2	tailward flows increase
08:19:50	far tail	P1	magnetic structures
08:20:10	far tail	P2	magnetic structures
08:33:00	far tail	P1,2	tailward flows cease

they reach the dawn-dusk terminator, then they accelerate to the solar wind speed in the tail. To extend the timing analysis in the tail to the global system, we assume a flow speed in the magnetosheath of -100 km/sec, as was observed by the MMS spacecraft. Once the flow reaches the dawn-dusk terminator, it will have accelerated again to near the solar wind speed of -540 km/sec. Therefore, from the magnetopause to X = 0, we assume the flow speed to be the midpoint of the magnetosheath speed and the solar wind speed, -220 km/sec. Table 4.2 summarizes the flow speeds and resultant propagation delays for each region.

Table 4.2: Summary of locations, flow speeds, and time delays for timing analysis.

Initial Point	X_i [R_E]	Final Point	X_f [R_E]	Flow Speed [km/sec]	Time Delay [min]
Geotail	17.5	bow shock	15	540	1.3
bow shock	15	magnetopause	10.8	100	4.5
magnetopause	10.8	terminator	0	220	5.2
terminator	0	reconnection site	-33.2	540	6.5

In the simulation results, a steady-state reconnection site is seen to develop around 07:40, indicating that a large enough amount of magnetic flux

accumulated in the tail between the start of the simulation at 07:15 and 07:39. This is in disagreement with the actual observations, in which flux could accumulate in the tail from the initial southward turning observed at the bow shock nose at 07:00 until the slow northward turning at 07:45, yet substorm onset did not occur until around 08:15. Therefore, the question remains as to why the actual magnetosphere did not reconfigure if enough energy to trigger a substorm had been stored earlier, as the model suggests. Though there was not a component at around 8:00 which could have triggered the substorm, a persistent southward IMF and large solar wind flow speed was observed from 07:00 to 07:40. The high dynamic pressure acting upon the magnetosphere during this interval would have caused a large amount of magnetic flux to accumulate in the tail, thus driving the system to a state in which as substorm was imminent. The weakening negative or positive B_z component after 07:40 did not provide enough of a disturbance to actually trigger the substorm and the system remained in a marginally unstable state.

Considering the determined propagation time from the Geotail satellite to the mid-tail of 17.5 minutes, we estimate that the packet which would have arrived at the mid-tail at the time of reconnection (08:14) would have been observed at Geotail around 07:56. As noted previously, however, the IMF observed at Geotail turns northward at 07:52 and is near zero between 07:40 and 07:52. In the absence of a strong, southward IMF immediately before the substorm onset, we consider the signatures in the magnetopause as a possible substorm trigger.

4.0.2 Magnetopause Signatures

During the intervals of southward IMF and large dynamic pressure, we propose that the magnetosphere was driven to a marginally unstable state in which a substorm is imminent. At that time, a maximum amount of energy had been stored in the magnetotail, but this amount had not been exceeded,

so the system did not reconfigure to a lower energy state. Then, at 08:00, the localized but large-amplitude signature observed in the magnetosheath is associated with the final trigger which initiated the substorm. Considering the 12-13 minute propagation delay to the midtail, the disconnected field at the dayside would arrive at the midtail at between 08:13 and 08:14. The additional magnetic flux in the tail would be enough to exceed the magnetotail storage limit and the substorm would be triggered. It is unlikely that the short-duration structure observed by MMS would produce a substorm without prior driving of the magnetosphere, as there would be an insufficient amount of magnetic flux accumulated in the tail. For this event, it is the combination of the strong dynamic pressure and southward IMF from 07:00 - 07:45 UT which destabilizes the magnetosphere and then the sudden pulsations with negative B_z in the magnetosheath which initiates reconnection.

It is significant to note the presence of mirror mode structures in the minutes prior to 08:00 observed by MMS. Mirror mode structures are non-propagating instabilities which have a characteristic anticorrelation between the magnetic field strength and the pressure. *Treumann et al.* (2004) reports that the mirror mode can violate the frozen-in condition and could therefore cause collisionless reconnection. Particles trapped within mirror mode structures produce a diamagnetic effect. In the vicinity of an X-line, this effect could annihilate the local magnetic field, thereby breaking the frozen-in condition and causing collisionless, but not necessarily resistive, reconnection. MMS was in close proximity to the dayside magnetopause where we expect reconnection to occur. The observed mirror mode instability could be an important phenomenon which initiated reconnection in the dayside, setting off a chain of events which eventually resulted in a global substorm.

We propose several possible explanations for the strong pulsations observed by MMS.

(1) The packets could be a smaller-scale structure in the solar wind which was not observed by Geotail, ACE, or OMNI. When passing through the bow

shock, the field magnitudes in the structure could have been increased by a typical shock compression value of 4, which would explain the very large magnitude of the pulsations. If smaller-scale structures can affect the onset and evolution of global magnetospheric processes, this will drive the need for an expanded array of solar wind monitoring missions. Considering that none of the solar wind monitors observed such a possible structure, such an effect could not have been predicted in the model.

(2) The pulsations could have been formed by a kinetic shock process due to a solar wind discontinuity hitting the bow shock. If it could be shown that this is the case, this result would suggest the importance of including shock physics in global MHD models, which currently are not present.

(3) It is possible that MMS briefly entered the magnetopause boundary and observed ongoing flux-transfer event (FTE) activity. The simulation results elucidate this possibility, as the results show the magnetopause nose distance increasing from 10.5 to 11.0 R_E between 07:50 and 08:10. MMS1 was located at a distance of 10.8 R_E at this time, so it is possible that it briefly entered but did not cross the boundary. The plasma and field values before and after the interval of interest are consistent with typical magnetosheath values, so the satellites did not completely cross the boundary for a substantial period of time. The observed pulsations could have been produced by a process at the boundary. The Z_{GSM} coordinate for MMS was negative, so it is possible that the mostly radial IMF at around 7:55, with negative $B_x \approx$ -4 nT, small negative B_y ($\approx$ -2 nT), and with B_z close to 0 nT produced a strongly anti-parallel field when convected through the dayside magneotsheath and draped around the magnetopause at $Z < 0$. MMS observed a magnetosheath velocity $\approx$ 100 km/sec, so it would take the IMF parcel observed by Geotail about 10 minutes to reach the magnetopause in the vicinity of MMS. The produced FTEs traveling in the positive Z-direction which passed by the MMS spacecraft. Indeed, these bursts of strong B_z fluctuations are associated with simultaneous magnetosheath and magnetospheric-like energy

population and positive v_z values. The plasma densities range from 20-30 cm^{-3} when the higher energy population is present. The colder component plasma in these fluctuations has even higher densities of 50-60 cm^{-3}. The relatively high densities could be associated with a cold plasmaspheric plume (e.g., *Elphic et al.*, 1996; *Goldstein et al.*, 2003), which has been shown to affect the dayside reconnection dynamics. This configuration, in which dense plasma from the plume reconnects with the magnetosheath plasma, is called asymmetric reconnection (*Cassak and Shay*, 2007). Several studies (*Walsh et al.*, 2014a,b) have shown that when a plasmaspheric plume is present, the reconnection jets have lower velocities and larger densities. The higher densities decrease the reconnection rate, indicating a weakening of the solar wind-magnetosphere coupling.

If these pulsations are not sufficient to cause reconnection at the dayside, then the questions remain as to what triggered the substorm, considering that no southward IMF was present for approximately 30 minutes prior to the onset time. A more in-depth analysis of the pulsations observed by MMS to discern between the possible explanations is left for future studies.

4.0.3 3-Dimensional Consideration

Throughout this discussion, the substorm events have been considered only in the X-Z plane. This simplification is commonly made in similar studies out of necessity because multipoint measurements are only available with regularly spacing along the X axis. Though the primary motion of substorm related phenomena (plasmoids, dipolarization fronts, X-line retreat, etc) is along or parallel to the Earth-Sun line, propagation distances in the Y or Z directions can be non-trivial (e.g. *Liu et al.*, 2011). Though the THEMIS and ARTEMIS probes have limited azimuthal and vertical separation, the simulation results indicate that the tail was shifted to the dusk flank, with the center of the X-line located at Y $\approx 4\ R_E$ at the downtail distance of X $\approx 53\ R_E$ (see Figure 3.4). This corresponds to approximately 23.7 MLT. In

Section 2.3, ground signatures were used to identify the central meridian of the substorm current wedge to be in between the PTRS and FSIM stations, corresponding to the ionospheric footprint of the near-Earth THEMIS probes and around 23 MLT. The reconnection outflows near the X-line have a limited azimuthal and vertical extent, but expand in these directions as they move tailward or earthward. As mentioned in the Introduction, many ongoing numerical studies of reconnection microphysics must consider the full 3-D geometry, which is considerably more complex than the 2-D simplification may suggest. Whereas MMS is well designed to study the 3-D reconnection physics at the microscale, macroscale missions such as THEMIS and ARTEMIS are not designed to collect multipoint measurements across the tail. Though the azimuthal extent and propagation of plasmoids and dipolarization fronts have not been studied extensively, these effects are likely small.

Chapter 5

Conclusion

We have presented observations of the 25 December 2015 substorm and traced the flow of energy from the solar wind and dayside magnetosheath to the near-Earth magnetosphere, tail region at lunar orbit, and to the ground. We have modeled the event using global MHD simulations and shown good, qualitative agreement, with the model and observations differing significantly only in the time at which reconnection occurred. Although much work is still required to fully understand the global substorm phenomenon, we present the following summary statements and conclusions for this case study of the 25 December 2015 event.

(1) Timing analysis conducted on the ARTEMIS and THEMIS data reveals a reconnection site near 33 R_E and a reconnection time around 08:14. This is consistent with previous work which applied timing methods to measurements collected with much smaller probe separations. The onset time of Pi2 pulsations and auroral activity on the ground corroborates the determined reconnection onset time and location.

(2) Solar wind observations before the onset time do not show the classical southward IMF condition associated with substorms. We conclude that persistent southward IMF approximately one hour before the substorm loaded the magnetosphere with energy in the form of magnetic flux, constituting the

substorm growth phase. This event is unique in that the expansion phase did not immediately follow the growth phase. Rather, the magnetotail remained in an unsteady state for approximately 30 minutes. This leads to many research questions to be considered in future studies: Why did the substorm not occur during the interval of southward IMF, as occurred in the simulation? For how long could the magnetosphere remain in this loaded state?

(3) The signatures observed at MMS occurred at a reasonable time to have eventually triggered substorm onset in the tail. Though analysis which would reveal the nature of these signatures is beyond the scope of the thesis, we conclude that the pulsations are closely related to triggering reconnection at the magnetopause, whether through strong southward magnetic pulses or mirror mode instabilities driving collisionless reconnection. The origin of these pulses could indicate that the current solar wind monitoring observatories are insufficient and/or that global MHD models should be improved to consider kinetic processes which occur at the bow shock. The results of the 25 December 2015 substorm case study will have important implications for future solar wind monitoring missions and global space weather modeling efforts.

Appendix

multimission_pos_xz.pro

Purpose: produces a plot of probe positions and field line traces in the XZ plane

```
; Miles Bengtson
; EP700
; March 1, 2017
; Plot XZ Locations of MMS, THEMIS, ARTEMIS, and RBSP

compile_opt idl2

axisthick = 2.0
charthick = 1.0
linethick = 2.0
charsize = 2.0
symsize = 1.0
A = FINDGEN(17) * (!PI*2/16.) ;makes a circular symbol to mark spacecraft
    position
USERSYM, COS(A), SIN(A), /FILL

timespan,'2015-12-25'
date='2015-12-25/08:15:00'

compile_opt idl2
thm_init

;===== THEMIS/ARTEMIS =====;
thm_init
probes=['a','b','c','d','e']
colors=['b','r','g','b','b']  ;colors for probes
thm_load_state,probe=probes,coord='gsm'
tkm2re,'th'+probes+'_state_pos',/replace
```

```
;===== MMS =====;
mms_load_state,probes='1',level='def',datatypes='pos'
tkm2re,'mms1_defeph_pos',/replace
mms_qcotrans,'mms1_defeph_pos',out_suffix='_gsm'
get_data,'mms1_defeph_pos_gsm',data=mms
tmp = min(abs(mms.x - time_double(date)),mms_pos)

;===== GEOTAIL =====;
; Select a text file and open for reading
file = '/home2/miles/data/geotail/20151225_mom_2115.txt'
;sTemplate = ASCII_TEMPLATE()
;SAVE,sTemplate,FILENAME='/home2/miles/data/geotail/
    geotail_mom_ascii_template.sav'
RESTORE, '/home2/miles/data/geotail/geotail_mom_ascii_template.sav'

geotaildata = READ_ASCII(file,TEMPLATE=sTemplate)
geotail_string = string(geotaildata.year)+"-"+string(geotaildata.month)+"-"+
    string(geotaildata.day)+"/"+string(geotaildata.hour)+":"+string(
    geotaildata.minute)+":"+string(geotaildata.second)
geotail_time = time_double(geotail_string)
geotail_pos = fltarr(n_elements(geotaildata.x),3)
geotail_pos[*,0] = geotaildata.x
geotail_pos[*,1] = geotaildata.y
geotail_pos[*,2] = geotaildata.z
store_data,'geotail_pos',geotail_time,geotail_pos

tmp = min(abs(geotail_time - time_double(date)),gt_pos)

;===== MOON =====;
thm_load_slp,trange=['2015-12-25','2015-12-26']
cotrans,'slp_lun_pos','slp_lun_pos_gse',/gei2gse
cotrans,'slp_lun_pos_gse','slp_lun_pos_gsm',/gse2gsm
tkm2re,'slp_lun_pos_gsm',/replace
get_data,'slp_lun_pos_gsm',data=moon
tmp = min(abs(moon.x - time_double(date)),moon_pos)

;===== TSY TRACE =====;
x = [-22,-22,-22,-22,-17,-12,-8,-5,-3,2,4,7,8,8]
y = replicate(0,14)
z = [10,7,4,0,replicate(0,9),4]

times = replicate(time_double(date),14)

trace_pts_north =  [[x],[y],[z]]
trace_pts_south =  [[x],[y],[-1*z]]
```

```
store_data,'trace_pts_north',data={x:times,y:trace_pts_north}
store_data,'trace_pts_south',data={x:times,y:trace_pts_south}

model = 't89'
par = 2.0D ;

;trace the field lines
ttrace2iono,'trace_pts_north',trace_var_name = 'trace_n', $
external_model=model,par=par,in_coord='gsm',out_coord=$
'gsm'
ttrace2iono,'trace_pts_south',trace_var_name = 'trace_s',$
external_model=model,par=par,in_coord='gsm',out_coord=$
'gsm', /south

;===== PLOT =====;
window,xsize=800,ysize=600

        ; MOON
tplotxy,'slp_lun_pos_gsm',versus='xrz',xrange=[-65,20],yrange=[-20,20]
plotxy,reform(moon.y[moon_pos,*],1,3),psym=2,symsize=symsize,versus='xrz',/
    over

        ; FIELD LINES
tplotxy,'trace_n2',versus='xrz',/over
tplotxy,'trace_s2',versus='xrz',/over

        ; MMS
tplotxy,'mms1_defeph_pos_gsm',versus='xrz',color='m',/over
plotxy,reform(mms.y[mms_pos,*],1,3),psym=8,color='m',symsize=symsize,versus=
    'xrz',/over
print,'mms',reform(mms.y[mms_pos,*],1,3)

        ; GEOTAIL
tplotxy,'geotail_pos',versus='xrz',color='c',/over
plotxy,reform(geotail_pos[gt_pos,*],1,3),psym=8,color='c',symsize=symsize,
    versus='xrz',/over
print,'geotail_pos',reform(geotail_pos[gt_pos,*],1,3)

        ; THEMIS
;plot the probe positions
for i = 0,n_elements(probes) - 1 do begin

  probe = probes[i]
  color = colors[i]

  varname = 'th'+probe+'_state_pos'
```

```
  get_data,varname,data=d

  ;skip if no valid data on day
  if ~is_struct(d) then continue
  ; plot a circle at time of interest
  tmp = min(abs(d.x - time_double('2015-12-25/08:17:20')),probe_pos)

  tplotxy,varname,versus='xrz',color=color,/over
  plotxy,reform(d.y[probe_pos,*],1,3),psym=8,color=color,symsize=symsize,
      versus='xrz',/over
  print,probe,reform(d.y[probe_pos,*],1,3)
endfor

popen,'/home2/miles/idl_lib/myidl_spedas/plots/traj_plots/
    multimission_pos_xz',/encapsulated
tplotxy
pclose
end
```

multimission_pos_xy.pro

Purpose: produces a plot of probe positions and field line traces in the XY plane

```
; Miles Bengtson
; EP700
; November 9, 2016
; Plot XY Locations of MMS, THEMIS, ARTEMIS, and RBSP

compile_opt idl2

axisthick = 2.0
charthick = 1.0
linethick = 2.0
charsize = 2.0
symsize = 1.0
A = FINDGEN(17) * (!PI*2/16.) ;makes a circular symbol to mark spacecraft
    position
USERSYM, COS(A), SIN(A), /FILL

timespan,'2015-12-25'
date='2015-12-25/08:15:00'

;===== RBSP =====;
  ; INITIALIZE RBSP SPICE KERNEL
 ; rbsp_spice_init
  ;rbsp_spice_config
```

```
  ; LOAD AND PLOT RBSP DATA (note this only works for probe a currently)
 ; rbprobe = 'a'
  ;rbsp_load_state,probe=rbprobe,datatype='pos' ;this is in GSE by default
  ;cotrans,'rbspa_pos_gse','rbspa_pos_gsm',/gse2gsm
 ; cotrans,'rbspb_pos_gse','rbspb_pos_gsm',/gse2gsm
 ; tkm2re,'rbspa_pos_gsm',/replace
 ; tkm2re,'rbspb_pos_gsm',/replace
 ; get_data,'rbspa_pos_gsm',data=drba
 ; get_data,'rbspb_pos_gsm',data=drbb
 ; rba=drba.y
 ; rbb=drbb.y
 ; tmp = min(abs(drba.x - time_double(date)),rbaprobe_pos) ; this is used to
      mark the exact probe location at date
 ; tmp = min(abs(drbb.x - time_double(date)),rbbprobe_pos)

;===== THEMIS/ARTEMIS =====;
thm_init
probes=['a','b','c','d','e']
colors=['b','r','g','b','b']  ;colors for probes
thm_load_state,probe=probes,coord='gsm'
tkm2re,'th'+probes+'_state_pos',/replace

;===== MMS =====;
mms_load_state,probes='1',level='def',datatypes='pos'
tkm2re,'mms1_defeph_pos',/replace
mms_qcotrans,'mms1_defeph_pos',out_suffix='_gsm'
get_data,'mms1_defeph_pos_gsm',data=mms
tmp = min(abs(mms.x - time_double(date)),mms_pos)

;===== GEOTAIL =====;
; Select a text file and open for reading
file = '/home2/miles/data/geotail/20151225_mom_2115.txt'
;sTemplate = ASCII_TEMPLATE()
;SAVE,sTemplate,FILENAME='/home2/miles/data/geotail/
    geotail_mom_ascii_template.sav'
RESTORE, '/home2/miles/data/geotail/geotail_mom_ascii_template.sav'

geotaildata = READ_ASCII(file,TEMPLATE=sTemplate)
geotail_string = string(geotaildata.year)+"-"+string(geotaildata.month)+"-"+
    string(geotaildata.day)+"/"+string(geotaildata.hour)+":"+string(
    geotaildata.minute)+":"+string(geotaildata.second)
geotail_time = time_double(geotail_string)
geotail_pos = fltarr(n_elements(geotaildata.x),3)
geotail_pos[*,0] = geotaildata.x
geotail_pos[*,1] = geotaildata.y
```

```
geotail_pos[*,2] = geotaildata.z
store_data,'geotail_pos',geotail_time,geotail_pos

tmp = min(abs(geotail_time - time_double(date)),gt_pos)

;===== MOON =====;
thm_load_slp,trange=['2015-12-25','2015-12-26']
cotrans,'slp_lun_pos','slp_lun_pos_gse',/gei2gse
cotrans,'slp_lun_pos_gse','slp_lun_pos_gsm',/gse2gsm
tkm2re,'slp_lun_pos_gsm',/replace
get_data,'slp_lun_pos_gsm',data=moon
tmp = min(abs(moon.x - time_double(date)),moon_pos)

;===== TSY =====;
; Plot Tsyganenko model field line traces
; Generate trace points and time

model = 't89'
par = 2.0D ;

;points for this plot will be generated from an ellipse
h = -5  ;x coordinate of ellipse center
k = 0   ;y coordinate of ellipse center
a = 15 ; size of semimajor axis
b = 12 ; size of semiminor axis
t = !DPI*dindgen(20)/10.
x = h + a*cos(t)
y = k + b*sin(t)
z = replicate(0D,20)
times = replicate(time_double(date),20)

trace_pts =  [[x],[y],[z]]
store_data,'trace_pts',data={x:times,y:trace_pts}

;trace the field lines
ttrace2iono,'trace_pts',trace_var_name = 'trace_n2',$
  external_model=model,par=par,in_coord='gsm',out_coord=$
  'gse'

ttrace2iono,'trace_pts',trace_var_name = 'trace_s2',$
  external_model=model,par=par,in_coord='gsm',out_coord=$
  'gse',/south

;===== PLOT =====;
window,xsize=800,ysize=600
```

```
;tplotxy,'rbspa_pos_gse',versus='xry',color='c',xrange=[-65,15],yrange
    =[-15,15],title="XY Probe Locations",xthick=axisthick,ythick=axisthick,
    charthick=charthick
;tplotxy,'rbspb_pos_gse',versus='xry',color='c',/over
;plotxy,reform(drba.y[rbaprobe_pos,*],1,3),psym=8,color='c',symsize=symsize,
    versus='xry',/over
;plotxy,reform(drbb.y[rbbprobe_pos,*],1,3),psym=8,color='c',symsize=symsize,
    versus='xry',/over

        ; MOON
tplotxy,'slp_lun_pos_gsm',versus='xry',xrange=[-65,20],yrange=[-20,20] ;,/
    over
plotxy,reform(moon.y[moon_pos,*],1,3),psym=2,symsize=symsize,versus='xry',/
    over

        ; FIELD LINES
tplotxy,'trace_n2',versus='xry',/over
tplotxy,'trace_s2',versus='xry',/over,linestyle=2

        ; MMS
tplotxy,'mms1_defeph_pos_gsm',versus='xry',color='m',/over
plotxy,reform(mms.y[mms_pos,*],1,3),psym=8,color='m',symsize=symsize,versus=
    'xry',/over
print,'mms',reform(mms.y[mms_pos,*],1,3)
        ; GEOTAIL
tplotxy,'geotail_pos',versus='xry',color='c',/over
plotxy,reform(geotail_pos[gt_pos,*],1,3),psym=8,color='c',symsize=symsize,
    versus='xry',/over
print,'geotail_pos',reform(geotail_pos[gt_pos,*],1,3)

        ; THEMIS
;plot the probe positions
for i = 0,n_elements(probes) - 1 do begin

  probe = probes[i]
  color = colors[i]

  varname = 'th'+probe+'_state_pos'
  get_data,varname,data=d

  ;skip if no valid data on day
  if ~is_struct(d) then continue
  ; plot a circle at time of interest
  tmp = min(abs(d.x - time_double('2015-12-25/08:17:20')),probe_pos)

  tplotxy,varname,versus='xry',color=color,/over
```

```
  plotxy,reform(d.y[probe_pos,*],1,3),psym=8,color=color,symsize=symsize,
      versus='xry',/over
  print,probe,reform(d.y[probe_pos,*],1,3)
endfor

;===== Print plot =====;
popen,'/home2/miles/idl_lib/myidl_spedas/plots/traj_plots/
    multimission_pos_xy',/encapsulated
tplotxy
pclose
end
```

thm_moments_combined.pro

Purpose: loads THEMIS field and plasma data and produces a stack plot

```
; Miles Bengtson
; EP700
; Spring 2017
; Purpose:
;       Combine ESA and SST datasets and calculate plasma parameters and
    moments

compile_opt idl2

; Expand left margin to better accomodate labels
tplot_options, 'xmargin', [15,9]

; Set time and probe
probe = ['b','c','d','e']
trange = '2015-12-25/08:' + ['15','30']
timespan,trange

thm_init
; thm_make_AE

; Load magnetometer data
thm_load_fgm,probe=probe,datatype='fgl'

; Load support data for pitch-angle and gyrophase rotation
thm_load_state,probe=probe,coord='gei',/get_support,trange=trange
thm_load_fit,probe=probe,coord='dsl',trange=trange

; Load ESA/SST combined dataset for ions
esai_datatype = 'peir'
ssti_datatype = 'psif'
combinedi = thm_part_combine(probe='b',trange=trange,esa_datatype=
```

```
    esai_datatype,sst_datatype=ssti_datatype)
thm_part_products,dist_array=combinedi,outputs='moments'

combinedi = thm_part_combine(probe='c',trange=trange,esa_datatype=
    esai_datatype,sst_datatype=ssti_datatype)
thm_part_products,dist_array=combinedi,outputs='moments'

combinedi = thm_part_combine(probe='e',trange=trange,esa_datatype=
    esai_datatype,sst_datatype=ssti_datatype)
thm_part_products,dist_array=combinedi,outputs='moments'

evtoj = 1.602d-19
get_data,'thb_ptirf_ptens',data=thb_ptens
thb_pres = fltarr(n_elements(thb_ptens.y))
thb_pres = evtoj*1.0d9*1.0d6*(thb_ptens.y[*,0] + thb_ptens.y[*,1] +
    thb_ptens.y[*,2])/3d0 ; convert from eV/cm3 to nPa
store_data,'thb_pres',thb_ptens.x,thb_pres

get_data,'thc_ptirf_ptens',data=thc_ptens
thc_pres = fltarr(n_elements(thc_ptens.y))
thc_pres = evtoj*1.0d9*1.0d6*(thc_ptens.y[*,0] + thc_ptens.y[*,1] +
    thc_ptens.y[*,2])/3d0
store_data,'thc_pres',thc_ptens.x,thc_pres

get_data,'the_ptirf_ptens',data=the_ptens
the_pres = fltarr(n_elements(the_ptens.y))
the_pres = evtoj*1.0d9*1.0d6*(the_ptens.y[*,0] + the_ptens.y[*,1] +
    the_ptens.y[*,2])/3d0
store_data,'the_pres',the_ptens.x,the_pres

; Make plot
window
;ylim,'thb_ptirf_velocity',[-800,500]
ylim,'the_ptirf_density',[0,0.8],log=0
ylim,'thc_ptirf_density',[0,0.4],log=0
ylim,'thb_ptirf_density',[0,0.4],log=0
ylim,'thb_ptirf_velocity',[-900,300],log=0
ylim,'thc_ptirf_velocity',[-900,300],log=0
options,'thb_ptirf_velocity',labels=['Vx','Vy','Vz']
options,'thb_fgl',labels=['Bx','By','Bz']
options,'thc_ptirf_velocity',labels=['Vx','Vy','Vz']
options,'thc_fgl',labels=['Bx','By','Bz']
options,'the_ptirf_velocity',labels=['Vx','Vy','Vz']
options,'the_fgl',labels=['Bx','By','Bz']
tplot,['thb_fgl','thb_ptirf_velocity','thb_ptirf_density','thb_ptirf_avgtemp
    ','thb_pres','thc_fgl','thc_ptirf_velocity','thc_ptirf_density','
```

```
    thc_ptirf_avgtemp','thc_pres','the_fgl','the_ptirf_velocity','
    the_ptirf_density','the_ptirf_avgtemp','the_pres']

;tplot,['thb_fgl','thb_ptirf_velocity','thc_fgl','thc_ptirf_velocity','
    the_fgl','the_ptirf_velocity']
; print to eps file
;popen,'/home2/miles/idl_lib/myidl_spedas/plots/pa_plots/thm_combined_stack
    ',/encapsulated,xsize=8,ysize=10,units='inches'
;tplot
;pclose


end
```

thm_energy_combined.pro

Purpose: loads THEMIS field, pitch angle, and energy data and produces a stack plot

```
; Miles Bengtson
; EP700
; Spring 2017
; Purpose:
;       Combine ESA and SST datasets and calculate Ti/Te ratio and Pitch
    Angle distributions


compile_opt idl2

; Expand left margin to better accomodate labels
tplot_options, 'xmargin', [15,9]

; Set time and probe
probe = 'b'
trange = '2015-12-25/08:' + ['15','45']
timespan,trange

; Load magnetometer data
thm_load_fgm,probe=probe,datatype='fgl'

; Load support data for pitch-angle and gyrophase rotation
thm_load_state,probe=probe,coord='gei',/get_support,trange=trange
thm_load_fit,probe=probe,coord='dsl',trange=trange

; Load ESA/SST combined dataset for ions
esai_datatype = 'peir'
ssti_datatype = 'psif'
```

```
combinedi = thm_part_combine(probe=probe,trange=trange,esa_datatype=
    esai_datatype,sst_datatype=ssti_datatype)

thm_part_products,dist_array=combinedi,outputs='energy'
thm_part_products,dist_array=combinedi,outputs='moments'
thm_part_products,dist_array=combinedi,outputs='pa'

; Load ESA/SST combined dataset for electrons
esae_datatype = 'peer'
sste_datatype = 'psef'
combinede = thm_part_combine(probe=probe,trange=trange,esa_datatype=
    esae_datatype,sst_datatype=sste_datatype)
thm_part_products,dist_array=combinede,outputs='moments'

thm_part_products,dist_array=combinede,outputs='energy'
thm_part_products,dist_array=combinede,outputs='moments'
thm_part_products,dist_array=combinede,outputs='pa'

; Compute TE/TI ratio
get_data,'thb_ptirf_avgtemp',data=di
get_data,'thb_pterf_avgtemp',data=de
tr = de.y/di.y
store_data,'thb_teti_ratio',di.x,tr

; Make plot
window
tplot,['thb_fgl','thb_teti_ratio','thb_ptirf_eflux_energy','
    thb_pterf_eflux_energy','thb_ptirf_eflux_pa','thb_pterf_eflux_pa']

; print to eps file
;popen,'/home2/miles/idl_lib/myidl_spedas/plots/pa_plots/thb_energy_combined
    ',/encapsulated,xsize=11,ysize=7,units='inches'
;tplot
;pclose


end
```

thm_limiting_pa.pro

Purpose: computes and plots the limiting pitch angle for THEMIS particle data

```
; Miles Bengtson
; EP700
; Limiting Pitch Angle Calculations
```

```
probe='b'
trange=['2015-12-25/08:15','2015-12-25/08:45']
timespan,trange
datatype = 'peir'
pi = 3.1415

;load support data for pitch-angle and gyrophase rotation
thm_load_state,probe=probe,coord='gei',/get_support,trange=trange
thm_load_fit,probe=probe,coord='dsl',trange=trange

;load particle data
thm_part_load,probe=probe,trange=trange,datatype=datatype
thm_part_products,probe=probe,datatype=datatype,trange=trange,outputs='pa'

;load magnetic field data
thm_load_fgm,probe=probe,datatype='fgl'

;load particle velocity
thm_load_esa,probe=probe,datatype='peir_velocity_gsm'

get_data,'thb_fgl',data=B

B2 = sqrt(B.y(*,0)^2+B.y(*,1)^2+B.y(*,2)^2)
ind = where(B2 eq max(B2)) ; use B1 as maximum of magnitude of B
;ind = where(B.y(*,0) eq max(B.y(*,0))) ; use B1 as maximum of Bx
B1 = sqrt(B.y(ind,0)^2 + B.y(ind,1)^2 + B.y(ind,2)^2)

alpha = 180*asin(sqrt(B2/B1(0)))/pi
temp = 90 - alpha
alpha1 = 90 + temp

store_data,'thb_alpha',B.x,alpha
store_data,'thb_alpha1',B.x,alpha1
ylim,'thb_alpha',0,180
ylim,'thb_alpha1',0,180
tplot,['thb_peir_velocity_dsl','thb_fgl','thb_peir_eflux_pa','thb_alpha','
    thb_alpha1']

; print to eps file
popen,'/home2/miles/idl_lib/myidl_spedas/plots/pa_plots/thb_limiting_pa',/
    encapsulated,xsize=11,ysize=7,units='inches'
tplot
pclose

end
```

thm_ionotrace.pro

Purpose: computes field line traces of THEMIS P3-P5 and plots ionospheric footprints along with ground-based observatory locations

```
; Miles Bengtson
; EP700
; Spring 2017
; THEMIS trace probe location to ionosphere and plot along with GMAG
    stations

compile_opt idl2

;sets background and color table
thm_init

date = '2015-12-28/08:17:00' ;date to be plotted
hrs = 12  ;specifies the interval over which data will be loaded
         ;this mainly has an effect on the amount of position
         ;data that will be loaded and plotted

sdate = time_double(date)-3600*hrs/2
edate = time_double(date)+3600*hrs/2

timespan,sdate,hrs,/hour

;Uncomment this code to use t01 model(or t96 or ts04)
model = 't96' ;set = to 't96' or 't04s' to use other models
kyoto_load_dst
omni_hro_load
;
tdegap,'kyoto_dst',/overwrite
tdeflag,'kyoto_dst','linear',/overwrite

tdegap,'OMNI_HRO_1min_BY_GSM',/overwrite
tdeflag,'OMNI_HRO_1min_BY_GSM','linear',/overwrite

tdegap,'OMNI_HRO_1min_BZ_GSM',/overwrite
tdeflag,'OMNI_HRO_1min_BZ_GSM','linear',/overwrite

tdegap,'OMNI_HRO_1min_proton_density',/overwrite
tdeflag,'OMNI_HRO_1min_proton_density','linear',/overwrite

tdegap,'OMNI_HRO_1min_flow_speed',/overwrite
tdeflag,'OMNI_HRO_1min_flow_speed','linear',/overwrite

store_data,'omni_imf',data=['OMNI_HRO_1min_BY_GSM','OMNI_HRO_1min_BZ_GSM']
```

```
;get_tsy_params generates parameters for t96,t01, & t04s models
get_tsy_params,'kyoto_dst','omni_imf',$
  'OMNI_HRO_1min_proton_density','OMNI_HRO_1min_flow_speed',model,/speed,/
      imf_yz

par = model + '_par'

colors=['m','g','c','b']  ;colors for probes
probes = ['a','c','d','e']

A = FINDGEN(17) * (!PI*2/16.) ;makes a circular symbol to mark spacecraft
    position
USERSYM, COS(A), SIN(A), /FILL

set_plot,'ps'
device,file='ionoplot.eps',/encapsulated

;generate a grid with MLT on it
aacgm_plot,local_time='2015-12-25/08:17:00',map_scale=52e6,thick=linethick,
    mlinethick=linethick,charthick=charthick,charsize=charsize,/noborder

;load spacecraft position
thm_load_state,probe=probes,coord='geo'

time_clip,'th?_state_pos',sdate,edate,/replace

;trace footpoints and label
for i = 0,n_elements(probes)-1 do begin

  probe=probes[i]
  color=(get_colors(colors[i]))[0]

  outname = 'th'+probe+'_ifoot'

  ttrace2iono,'th'+probe+'_state_pos',external_model=model,/km, par=par,
      in_coord='geo',out_coord='geo',newname=outname

  xyz_to_polar,outname

  get_data,outname+'_phi',data=d

  ;skip if data doesn't exist
  if ~is_struct(d) then continue

  i_lon=d.y
```

```
  get_data,outname+'_th',data=d

  i_lat=d.y

  plots,i_lon,i_lat,color=color,thick=linethick

  tmp = min(abs(d.x - time_double(date)),probe_pos)

  plots,i_lon[probe_pos],i_lat[probe_pos],psym=8,color=color,symsize=symsize
      ,thick=linethick

endfor

;This section overplots ground station position on the map
;get groundstation positions
thm_asi_stations,labels,locations

labels = ['FSMI','GILL','FSIM','PTRS','WHIT','INUV','FYKN','POKR']
locations = [[59.984 ,  248.158 ],[56.354 ,  265.344 ],[61.762 ,  238.779
    ],[56.810, 227.050 ],[61.010 , 224.777 ],[68.413 ,  226.230 ],[66.560 ,
     214.786 ],[65.119, 212.567 ]]

;for stations not in this list, you'll need to look up the location
for i = 0,8-1 do begin

  print,labels[i]
  plots,locations[1,i],locations[0,i],psym=6,color=(i mod 7)+1,symsize=
      symsize,thick=linethick

endfor

device,/close
end
```

timing_contour_plots.m

Purpose: calculates reconnection site location and onset time for a range of flow speeds and produces contour plots

```
% Miles Bengtson
% Reconnection Site and Timing Location
% Contour Plots
% EP700
% Spring 2017

clear;
```

```
clc;
close all;

Re = 6370; % km
min2sec = 60;

xe = -11;
te = 4*min2sec; % define 0813 as t0 and flows were observed at 0817
xt = -58.3;
tt = 4*min2sec;

% vt = linspace(600,1200); % range of tailside MS speeds in km/sec
% ve = linspace(200,800); % range of earthside MS speeds in km/sec

[ve,vt] = meshgrid(linspace(600,1200,1000),linspace(200,800,1000));
vtre = vt/Re;
vere = ve/Re;

tr = (xt + vere*te + vtre*tt - xe)./(vere + vtre);
xr = xt + vtre.*(tt - tr);

figure;
[c1,h1] = contour(ve,vt,tr);
clabel(c1,h1);
set(h1,'LineWidth',2)
set(gca,'FontSize',13)
title('Reconnection Time [seconds after 0813 UT]');
xlabel('V_{Earth} [km/sec]');
ylabel('V_{Tail} [km/sec]');

figure;
[c2,h2] = contour(ve,vt,xr);
clabel(c2,h2);
set(h2,'LineWidth',2)
set(gca,'FontSize',13)
title('Reconnection Site [RE]');
xlabel('V_{Earth} [km/sec]');
ylabel('V_{Tail} [km/sec]');
```

thm_pi2_pulsations.pro

Purpose: loads and plots AE index, all-sky imager, and ground magnetometer data

```
; Miles Bengtson
; EP700
; Spring 2017
```

```
; THEMIS GMAG Pi2 Pulsations load, calculate, and plot routine

timespan,['2015-12-25/08','2015-12-25/08:40']

thm_init
thm_make_ae

site = ['gill','fsmi','fsim','ptrs','whit','inuv','fykn','pokr'] ; arranged
    E to W

thm_load_gmag,site=site,trange=trange,/subtract_median

site_asi = ['fsmi']
thm_load_asi,site=site_asi,datatype='asf'

get_data,'thg_asf_fsmi',data=d
totals=total(total(d.y,2),2)
store_data,'fsmi_tot',data={x:d.x,y:totals-min(totals)}

tplot,['thmAE','fsmi_tot','thg_mag_'+site]
timebar,time_double('2015-12-25/08:17:45')
;tplot,site_asi+'_tot'

popen,'/home2/miles/idl_lib/myidl_spedas/plots/asi_plots/geom_data',/
    encapsulated,xsize=8,ysize=10,units='inches'
tplot
pclose

end
```

solar_wind_data.pro

Purpose: loads and plots field and plasma data for Geotail, OMNI, and ACE

```
; Miles Bengtson
; EP700
; Spring 2017

;===== DEFINE CONSTANTS =====;
evtok = 11604 ; eV to K conversion
ktoev = 8.6177d-5 ; K to eV conversion
k = 1.38065d-23 ; Boltzmann's Constant in J/K

;===== LOAD GEOTAIL DATA =====;
        ;LOAD MAGNETIC FIELD DATA
file2 = '/home2/miles/data/geotail/20151225_mag_20421.txt'
RESTORE, '/home2/miles/data/geotail/geotail_mag_ascii_template.sav'
```

```
geotailbdata = READ_ASCII(file2,TEMPLATE=mTemplate)
geotailb_string = string(geotailbdata.year)+"-"+string(geotailbdata.month)
    +"-"+string(geotailbdata.day)+"/"+string(geotailbdata.hour)+":"+string(
    geotailbdata.minute)+":"+string(geotailbdata.second)

geotail_time = time_double(geotailb_string)
geotail_b = fltarr(n_elements(geotailbdata.bx),3)
geotail_b[*,0] = geotailbdata.bx
geotail_b[*,1] = geotailbdata.by
geotail_b[*,2] = geotailbdata.bz

        ;LOAD PARTICLE MOMENT DATA
file = '/home2/miles/data/geotail/20151225_mom_20421.txt'
RESTORE, '/home2/miles/data/geotail/geotail_mom_ascii_template.sav'

geotailvdata = READ_ASCII(file,TEMPLATE=sTemplate)
geotail_string = string(geotailvdata.year)+"-"+string(geotailvdata.month)
    +"-"+string(geotailvdata.day)+"/"+string(geotailvdata.hour)+":"+string(
    geotailvdata.minute)+":"+string(geotailvdata.second)

geotailv_time = time_double(geotail_string)
geotail_v = fltarr(n_elements(geotailvdata.v_x),3)
geotail_v[*,0] = geotailvdata.v_x
geotail_v[*,1] = geotailvdata.v_y
geotail_v[*,2] = geotailvdata.v_z
store_data,'geotail_v',geotailv_time,geotail_v

Ti = 0.5*(geotailvdata.Tiyy + geotailvdata.Tizz) ;find total ion temperature

        ;INTERPOLATE MOMENT DATA ONTO MAGNETIC FIELD GRID
geotail_vx = interpol(geotailvdata.v_x,geotailv_time,geotail_time)
geotail_vy = interpol(geotailvdata.v_y,geotailv_time,geotail_time)
geotail_vz = interpol(geotailvdata.v_z,geotailv_time,geotail_time)
geotail_n = interpol(geotailvdata.density,geotailv_time,geotail_time)
geotail_temp = interpol(Ti,geotailv_time,geotail_time)
geotail_p = (geotail_n*100d0^3)*k*(geotail_temp*evtok)*10d0^9 ; plasma
    pressure
store_data,'geotail_vx',geotail_time,geotail_vx
store_data,'geotail_vy',geotail_time,geotail_vy
store_data,'geotail_vz',geotail_time,geotail_vz
store_data,'geotail_bx',geotail_time,geotailbdata.bx
store_data,'geotail_by',geotail_time,geotailbdata.by
store_data,'geotail_bz',geotail_time,geotailbdata.bz
store_data,'geotail_n',geotail_time,geotail_n
store_data,'geotail_temp',geotail_time,geotail_temp
```

```
store_data,'geotail_p',geotail_time,geotail_p

;===== LOAD OMNI DATA =====;
file3 = '/home2/miles/data/omni.txt'
;oTemplate = ASCII_TEMPLATE()
;SAVE,oTemplate,FILENAME='/home2/miles/data/omni_ascii_template.sav'
RESTORE, '/home2/miles/data/omni_ascii_template.sav'
omni = READ_ASCII(file3,TEMPLATE=oTemplate)

omni_string = '2015-12-25/'+string(omni.hr)+':'+string(omni.mn)+':00'
omni_t = time_double(omni_string)


;===== LOAD ACE DATA =====;
file4 = '/home2/miles/data/ace.txt'
;aTemplate = ASCII_TEMPLATE()
;SAVE,aTemplate,FILENAME='/home2/miles/data/ace_ascii_template.sav'
RESTORE, '/home2/miles/data/ace_ascii_template.sav'
ace = READ_ASCII(file4,TEMPLATE=aTemplate)

ace_string = '2015-12-25/'+string(ace.hr)+':'+string(ace.min)+':00'
ace_t = time_double(ace_string)

;===== SAVE OMNI/ACE DATA TOGETHER =====;
;===== V COMPONENTS =====;
omni_ace_vx = fltarr(n_elements(omni.vx),2)
omni_ace_vx[*,0] = omni.vx
omni_ace_vx[*,1] = ace.vx
ind = where(omni_ace_vx GT 10000)
omni_ace_vx[ind] = 'NaN'
store_data,'omni_ace_vx',ace_t,omni_ace_vx

omni_ace_vy = fltarr(n_elements(omni.vy),2)
omni_ace_vy[*,0] = omni.vy
omni_ace_vy[*,1] = ace.vy
ind = where(omni_ace_vy GT 10000)
omni_ace_vy[ind] = 'NaN'
store_data,'omni_ace_vy',ace_t,omni_ace_vy

omni_ace_vz = fltarr(n_elements(omni.vz),2)
omni_ace_vz[*,0] = omni.vz
omni_ace_vz[*,1] = ace.vz
ind = where(omni_ace_vz GT 10000)
omni_ace_vz[ind] = 'NaN'
store_data,'omni_ace_vz',ace_t,omni_ace_vz
```

```
;===== B COMPONENTS =====;
omni_ace_bx = fltarr(n_elements(omni.bx),2)
omni_ace_bx[*,0] = omni.bx
omni_ace_bx[*,1] = ace.bx
ind = where(omni_ace_bx GT 1000)
omni_ace_bx[ind] = 'NaN'
store_data,'omni_ace_bx',ace_t,omni_ace_bx

omni_ace_by = fltarr(n_elements(omni.by),2)
omni_ace_by[*,0] = omni.by
omni_ace_by[*,1] = ace.by
ind = where(omni_ace_by GT 1000)
omni_ace_by[ind] = 'NaN'
store_data,'omni_ace_by',ace_t,omni_ace_by

omni_ace_bz = fltarr(n_elements(omni.bz),2)
omni_ace_bz[*,0] = omni.bz
omni_ace_bz[*,1] = ace.bz
ind = where(omni_ace_bz GT 1000)
omni_ace_bz[ind] = 'NaN'
store_data,'omni_ace_bz',ace_t,omni_ace_bz

;===== DENSITY =====;
omni_ace_n = fltarr(n_elements(omni.n),2)
omni_ace_n[*,0] = omni.n
omni_ace_n[*,1] = ace.n
ind = where(omni_ace_n GT 100)
omni_ace_n[ind] = 'NaN'
store_data,'omni_ace_n',ace_t,omni_ace_n

;===== TEMPERATURE =====;
omni_ace_temp = fltarr(n_elements(omni.t),2)
omni_ace_temp[*,0] = omni.t*ktoev
omni_ace_temp[*,1] = ace.t*ktoev
ind = where(omni_ace_temp GT 800)
omni_ace_temp[ind] = 'NaN'
store_data,'omni_ace_temp',ace_t,omni_ace_temp

;===== PRESSURE =====;
omni_ace_p = fltarr(n_elements(omni.p),2)
omni_ace_p[*,0] = omni.p
;omni_ace_p[*,1] = (ace.n*100d0^3)*k*ace.t*10d0^9 ; P = nkT [nPa]
mp = 1.6726d-27
omni_ace_p[*,1] = ((ace.n*100d0^3)*k*ace.t + 0.5*mp*ace.n*100d03*(ace.vx
    *1000)^2)*10d0^9 ; dynamic pressure and kinetic pressure
ind = where(omni_ace_p GT 50)
```

```
omni_ace_p[ind] = 'NaN'
store_data,'omni_ace_p',ace_t,omni_ace_p

;===== MAKE PLOTS =====;
thm_init ; load themis colortable
timespan,['2015-12-25/07','2015-12-25/09']
options,'omni_ace_bx',colors=['g','r']
options,'omni_ace_bx',labels=['OMNI','ACE']
options,'omni_ace_bx','yrange',[-6,6]
options,'omni_ace_by',colors=['g','r']
options,'omni_ace_by',labels=['OMNI','ACE']
options,'omni_ace_by','yrange',[-6,6]
options,'omni_ace_bz',colors=['g','r']
options,'omni_ace_bz',labels=['OMNI','ACE']
options,'omni_ace_bz','yrange',[-6,6]
options,'omni_ace_vx',colors=['g','r']
options,'omni_ace_vx',labels=['OMNI','ACE']
options,'omni_ace_vx','yrange',[-580,-460]
options,'omni_ace_vy',colors=['g','r']
options,'omni_ace_vy',labels=['OMNI','ACE']
options,'omni_ace_vy','yrange',[-60,60]
options,'omni_ace_vz',colors=['g','r']
options,'omni_ace_vz',labels=['OMNI','ACE']
options,'omni_ace_vz','yrange',[-40,40]
options,'omni_ace_n',colors=['g','r']
options,'omni_ace_n',labels=['OMNI','ACE']
options,'omni_ace_n','yrange',[0,8]
options,'omni_ace_temp',colors=['g','r']
options,'omni_ace_temp',labels=['OMNI','ACE']
options,'omni_ace_temp','yrange',[0,70]
options,'omni_ace_p',colors=['g','r']
options,'omni_ace_p',labels=['OMNI','ACE']
options,'omni_ace_p','yrange',[0,5]
tplot,['omni_ace_bx','omni_ace_by','omni_ace_bz','omni_ace_vx','omni_ace_vy'
    ,'omni_ace_vz','omni_ace_n','omni_ace_temp','omni_ace_p']


popen,'/home2/miles/idl_lib/myidl_spedas/ccmc/sw_data',/encapsulated,xsize
    =8,ysize=10,units='inches'
tplot
pclose

options,'geotail_bx',colors=['b']
options,'geotail_bx',labels=['GEOTAIL']
options,'geotail_bx','yrange',[-6,6]
options,'geotail_by',colors=['b']
```

```
options,'geotail_by',labels=['GEOTAIL']
options,'geotail_by','yrange',[-6,6]
options,'geotail_bz',colors=['b']
options,'geotail_bz',labels=['GEOTAIL']
options,'geotail_bz','yrange',[-6,6]
options,'geotail_vx',colors=['b']
options,'geotail_vx',labels=['GEOTAIL']
options,'geotail_vx','yrange',[-580,-460]
options,'geotail_vy',colors=['b']
options,'geotail_vy',labels=['GEOTAIL']
options,'geotail_vy','yrange',[-60,60]
options,'geotail_vz',colors=['b']
options,'geotail_vz',labels=['GEOTAIL']
options,'geotail_vz','yrange',[-40,40]
options,'geotail_n',colors=['b']
options,'geotail_n',labels=['GEOTAIL']
options,'geotail_n','yrange',[0,8]
options,'geotail_temp',colors=['b']
options,'geotail_temp',labels=['GEOTAIL']
options,'geotail_temp','yrange',[0,70]
options,'geotail_p',colors=['b']
options,'geotail_p',labels=['GEOTAIL']
options,'geotail_p','yrange',[0,5]
;tplot,['geotail_bx','geotail_by','geotail_bz','geotail_vx','geotail_vy','
    geotail_vz','geotail_n','geotail_temp','geotail_p']

popen,'/home2/miles/idl_lib/myidl_spedas/ccmc/geotail_sw_data',/encapsulated
    ,xsize=8,ysize=10,units='inches'
tplot
pclose

end
```

mms_stack.pro

Purpose: loads and plots field and plasma data for MMS

```
; Miles Bengtson
; EP700
; Spring 2017
; Load MMS Data


trange = ['2015-12-25/07:50','2015-12-25/08:30']
timespan,['2015-12-25/07:50','2015-12-25/08:30']

probe = '1'
```

```
datatype = ['des-moms', 'dis-moms']  ; DES/DIS moments file (contains
    moments, as well as spectra and pitch angle distributions)
level = 'l2'
data_rate = 'fast'

mms_load_fgm, probe=probe, /time_clip
mms_load_fpi, probes = probe, datatype = datatype, level = level, data_rate
    = data_rate
;mms_load_eis, probes=probe, trange=trange, datatype='extof', level = level


cotrans,'mms1_fgm_b_gse_srvy_l2_bvec','mms1_fgm_b_gsm_srvy_l2_bvec',/gse2gsm
cotrans,'mms1_dis_prestensor_gse_fast','mms1_dis_prestensor_gsm_fast',/
    gse2gsm
cotrans,'mms1_dis_bulkv_gse_fast','mms1_dis_bulkv_gsm_fast',/gse2gsm

get_data,'mms1_dis_temppara_fast',data=para
get_data,'mms1_dis_tempperp_fast',data=perp

Ttot = 0.5*(para.y+perp.y) ; take average of components
store_data,'mms1_dis_temp_fast',para.x,Ttot

ylim,'mms1_dis_prestensor_gsm_fast',1.5,3.5
tplot, ['mms1_fgm_b_gse_srvy_l2_btot','mms1_fgm_b_gsm_srvy_l2_bvec','
    mms1_dis_prestensor_gsm_fast','mms1_dis_bulkv_gsm_fast','
    mms1_dis_numberdensity_fast', $
'mms1_dis_temp_fast','mms1_dis_energyspectr_omni_fast']

; print to eps file
popen,'/home2/miles/idl_lib/myidl_spedas/plots/mms_stack',/encapsulated,
    xsize=8,ysize=10,units='inches'
tplot
pclose

end
```

Bibliography

Akasofu, S.-I. (1964), The development of the auroral substorm, *Planetary and Space Science*, *12*(4), 273–282.

Angelopoulos, V. (2009), The THEMIS mission, in *The THEMIS Mission*, vol. 141, pp. 5–34, Springer.

Angelopoulos, V. (2011), The ARTEMIS mission, *Space science reviews*, *165*(1-4), 3–25.

Angelopoulos, V., C. F. Kennel, F. V. Coroniti, R. Pellat, M. G. Kivelson, R. J. Walker, C. T. Russell, W. Baumjohann, W. C. Feldman, and J. T. Gosling (1994), Statistical characteristics of bursty bulk flow events, *J. Geophys. Res.*, *99*, 21,257, doi:10.1029/94JA01263.

Angelopoulos, V., J. P. McFadden, D. Larson, C. W. Carlson, S. B. Mende, H. Frey, T. Phan, D. G. Sibeck, K.-H. Glassmeier, U. Auster, et al. (2008), Tail reconnection triggering substorm onset, *Science*, *321*(5891), 931–935.

Atkinson, G. (1967), An approximate flow equation for geomagnetic flux tubes and its application to polar substorms, *Journal of Geophysical Research*, *72*(21), 5373–5382.

Auster, H., K. Glassmeier, W. Magnes, O. Aydogar, W. Baumjohann, D. Constantinescu, D. Fischer, K. Fornacon, E. Georgescu, P. Harvey, et al. (2009), The THEMIS fluxgate magnetometer, in *The THEMIS Mission*, pp. 235–264, Springer.

Axford, W. (1999), Reconnection, substorms and solar flares, *Physics and Chemistry of the Earth, Part C: Solar, Terrestrial & Planetary Science*, *24*(1), 147–151.

Baker, D., T. Pulkkinen, M. Hesse, and R. McPherron (1997), A quantitative assessment of energy storage and release in the earth's magnetotail, *Journal of geophysical research*, *102*, 7159–7168.

Baker, D. N., T. Pulkkinen, V. Angelopoulos, W. Baumjohann, and R. McPherron (1996), Neutral line model of substorms: Past results and present view, *Journal of Geophysical Research: Space Physics*, *101*(A6), 12,975–13,010.

Birn, J., J. Drake, M. Shay, B. Rogers, R. Denton, M. Hesse, M. Kuznetsova, Z. Ma, A. Bhattacharjee, A. Otto, et al. (2001), Geospace environmental modeling (gem) magnetic reconnection challenge, *Journal of Geophysical Research: Space Physics*, *106*(A3), 3715–3719.

Biskamp, D., E. Schwarz, and J. F. Drake (1995), Ion-controlled collisionless magnetic reconnection, *Phys. Rev. Lett.*, *75*, 3850–3853, doi: 10.1103/PhysRevLett.75.3850.

Borovsky, J. E., R. J. Nemzek, and R. D. Belian (1993), The occurrence rate of magnetospheric-substorm onsets: Random and periodic substorms, *Journal of Geophysical Research: Space Physics*, *98*(A3), 3807–3813.

Burch, J., T. Moore, R. Torbert, and B. Giles (2016), Magnetospheric multiscale overview and science objectives, *Space Science Reviews*, *199*(1-4), 5–21.

Caan, M. N., R. L. McPherron, and C. T. Russell (1977), Characteristics of the association between the interplanetary magnetic field and substorms, *Journal of Geophysical Research*, *82*(29), 4837–4842.

Cassak, P., and M. Shay (2007), Scaling of asymmetric magnetic reconnection: General theory and collisional simulations, *Physics of Plasmas*, *14*(10), 102,114.

Dungey, J. (1950), A note on magnetic fields in conducting materials, in *Mathematical Proceedings of the Cambridge Philosophical Society*, vol. 46, pp. 651–654, Cambridge Univ Press.

Dungey, J. W. (1961), Interplanetary magnetic field and the auroral zones, *Physical Review Letters*, *6*(2), 47.

Elphic, R. C., L. A. Weiss, M. F. Thomsen, D. J. McComas, and M. B. Moldwin (1996), Evolution of plasmaspheric ions at geosynchronous orbit during times of high geomagnetic activity, *Geophysical Research Letters*, *23*(16), 2189–2192, doi:10.1029/96GL02085.

Fairfield, D. H. (1971), Average and unusual locations of the earth's magnetopause and bow shock, *Journal of Geophysical Research*, *76*(28), 6700–6716.

Fu, H., Y. V. Khotyaintsev, A. Vaivads, M. André, and S. Huang (2012), Occurrence rate of earthward-propagating dipolarization fronts, *Geophysical Research Letters*, *39*(10).

Gabrielse, C., V. Angelopoulos, A. Runov, H. Frey, J. McFadden, D. Larson, K.-H. Glassmeier, S. Mende, C. Russell, S. Apatenkov, et al. (2009), Timing and localization of near-earth tail and ionospheric signatures during a substorm onset, *Journal of Geophysical Research: Space Physics*, *114*(A1).

Giovanelli, R. (1947), Magnetic and electric phenomena in the sun's atmosphere associated with sunspots, *Monthly Notices of the Royal Astronomical Society*, *107*(4), 338–355.

Goldstein, J., B. R. Sandel, M. R. Hairston, and P. H. Reiff (2003), Control of plasmaspheric dynamics by both convection and sub-auroral polarization stream, *Geophysical Research Letters*, *30*(24), n/a–n/a, doi: 10.1029/2003GL018390, 2243.

Hasegawa, A. (1969), Drift mirror instability in the magnetosphere, *The Physics of Fluids*, *12*(12), 2642–2650.

Ieda, A., S. Machida, T. Mukai, Y. Saito, T. Yamamoto, A. Nishida, T. Terasawa, and S. Kokubun (1998), Statistical analysis of the plasmoid evolution with Geotail observations, *Journal of Geophysical Research: Space Physics*, *103*(A3), 4453–4465.

Kokubun, S., T. Yamamoto, M. H. Acuña, K. Hayashi, K. Shiokawa, and H. Kawano (1994), The GEOTAIL magnetic field experiment, *Journal of geomagnetism and geoelectricity*, *46*(1), 7–22.

Liu, J., V. Angelopoulos, H. Frey, J. McFadden, D. Larson, K. Glassmeier, S. Mende, C. Russell, I. Rae, K. Murphy, et al. (2009), THEMIS observation of a substorm event on 04: 35, 22 february 2008, in *Annales Geophysicae*, vol. 27, pp. 1831–1841, Copernicus GmbH.

Liu, J., V. Angelopoulos, M. Kubyshkina, J. McFadden, K.-H. Glassmeier, and C. Russell (2011), Revised timing and onset location of two isolated substorms observed by time history of events and macroscale interactions during substorms (THEMIS), *Journal of Geophysical Research: Space Physics*, *116*(A5).

Lui, A. (1996), Current disruption in the earth's magnetosphere: Observations and models, *Journal of Geophysical Research: Space Physics*, *101*(A6), 13,067–13,088.

McFadden, J., C. Carlson, D. Larson, M. Ludlam, R. Abiad, B. Elliott, P. Turin, M. Marckwordt, and V. Angelopoulos (2008), The THEMIS esa

plasma instrument and in-flight calibration, *Space Science Reviews*, *141*(1-4), 277–302.

McPherron, R. L., C. Russell, and M. Aubry (1973), Satellite studies of magnetospheric substorms on august 15, 1968: 9. phenomenological model for substorms, *Journal of Geophysical Research*, *78*(16), 3131–3149.

Mende, S., S. Harris, H. Frey, V. Angelopoulos, C. Russell, E. Donovan, B. Jackel, M. Greffen, and L. Peticolas (2009a), The THEMIS array of ground-based observatories for the study of auroral substorms, in *The THEMIS Mission*, pp. 357–387, Springer.

Mende, S., V. Angelopoulos, H. Frey, E. Donovan, B. Jackel, K.-H. Glassmeier, J. McFadden, D. Larson, and C. Carlson (2009b), Timing and location of substorm onsets from THEMIS satellite and ground based observations, in *Annales Geophysicae*, vol. 27, pp. 2813–2830, Copernicus GmbH.

Moldwin, M. B., and W. J. Hughes (1992), On the formation and evolution of plasmoids: A survey of ISEE-3 Geotail data, *Journal of Geophysical Research: Space Physics*, *97*(A12), 19,259–19,282.

Mukai, T., S. Machida, Y. Saito, M. Hirahara, T. Terasawa, N. Kaya, T. Obara, M. Ejiri, and A. Nishida (1994), The low energy particle (lep) experiment onboard the Geotail satellite, *Journal of geomagnetism and geoelectricity*, *46*(8), 669–692.

Nagai, T., R. Nakamura, T. Mukai, T. Yamamoto, A. Nishida, and S. Kokubun (1997), Substorms, tail flows and plasmoids, *Advances in Space Research*, *20*(4-5), 961–971.

Nishida, A. (1983), Imf control of the earth's magnetosphere, *Space Science Reviews*, *34*(2), 185–200.

Nishida, A., K. Uesugi, I. Nakatani, T. Mukai, D. Fairfield, and M. Acuna (1992), Geotail mission to explore earth's magnetotail, *Eos, Transactions American Geophysical Union*, *73*(40), 425–429.

Nykyri, K., A. Otto, E. Adamson, E. Kronberg, and P. Daly (2012), On the origin of high-energy particles in the cusp diamagnetic cavity, *Journal of Atmospheric and Solar-Terrestrial Physics*, *87*, 70–81.

Øieroset, M., T. D. Phan, R. P. Lin, and B. U. Sonnerup (2000), Walén and variance analyses of high-speed flows observed by wind in the midtail plasma sheet: Evidence for reconnection, *Journal of Geophysical Research: Space Physics*, *105*(A11), 25,247–25,263.

Øieroset, M., T. Phan, M. Fujimoto, R. Lin, and R. Lepping (2001), In situ detection of collisionless reconnection in the earth's magnetotail, *Nature*, *412*(6845), 414–417.

Oka, M., T.-D. Phan, J. Eastwood, V. Angelopoulos, N. Murphy, M. Øieroset, Y. Miyashita, M. Fujimoto, J. McFadden, and D. Larson (2011), Magnetic reconnection x-line retreat associated with dipolarization of the earth's magnetosphere, *Geophysical Research Letters*, *38*(20).

Parker, E. N. (1957), Sweet's mechanism for merging magnetic fields in conducting fluids, *Journal of Geophysical Research*, *62*(4), 509–520.

Petschek, H. E. (1964), Magnetic field annihilation, *NASA Special Publication*, *50*, 425.

Platino, M., and U. S. Inan (2001), Cluster ii, http://nova.stanford.edu/ vlf/-clusterII/clusterII.htm.

Pollock, C., T. Moore, A. Jacques, J. Burch, U. Gliese, Y. Saito, T. Omoto, L. Avanov, A. Barrie, V. Coffey, et al. (2016), Fast plasma investigation for magnetospheric multiscale, *Space Science Reviews*, *199*(1-4), 331–406.

Pu, Z., X. Chu, X. Cao, V. Mishin, V. Angelopoulos, J. Wang, Y. Wei, Q. Zong, S. Fu, L. Xie, et al. (2010), THEMIS observations of substorms on 26 february 2008 initiated by magnetotail reconnection, *Journal of Geophysical Research: Space Physics*, *115*(A2).

Richardson, I., and S. Cowley (1985), Plasmoid-associated energetic ion bursts in the deep geomagnetic tail: Properties of the boundary layer, *Journal of Geophysical Research: Space Physics*, *90*(A12), 12,133–12,158.

Rostoker, G., S.-I. Akasofu, J. Foster, R. Greenwald, Y. Kamide, K. Kawasaki, A. Lui, R. McPherron, and C. Russell (1980), Magnetospheric substorms—definition and signatures, *Journal of Geophysical Research: Space Physics*, *85*(A4), 1663–1668.

Runov, A., V. Angelopoulos, M. Sitnov, V. Sergeev, J. Bonnell, J. McFadden, D. Larson, K.-H. Glassmeier, and U. Auster (2009a), THEMIS observations of an earthward-propagating dipolarization front, *Geophysical Research Letters*, *36*(14).

Runov, A., V. Angelopoulos, V. Sergeev, K. Glassmeier, U. Auster, J. McFadden, D. Larson, and I. Mann (2009b), Global properties of magnetotail current sheet flapping: THEMIS perspectives, in *Annales geophysicae: atmospheres, hydrospheres and space sciences*, vol. 27, p. 319.

Runov, A., V. Angelopoulos, X.-Z. Zhou, X.-J. Zhang, S. Li, F. Plaschke, and J. Bonnell (2011), A THEMIS multicase study of dipolarization fronts in the magnetotail plasma sheet, *Journal of Geophysical Research: Space Physics*, *116*(A5).

Russell, C., P. Chi, D. Dearborn, Y. Ge, B. Kuo-Tiong, J. Means, D. Pierce, K. Rowe, and R. Snare (2008), THEMIS ground-based magnetometers, in *The THEMIS Mission*, pp. 389–412, Springer.

Russell, C., B. Anderson, W. Baumjohann, K. Bromund, D. Dearborn, D. Fischer, G. Le, H. Leinweber, D. Leneman, W. Magnes, et al. (2014), The magnetospheric multiscale magnetometers, *Space Science Reviews*, *199*(1-4), 189–256.

Saito, T. (1969), Geomagnetic pulsations, *Space Science Reviews*, *10*(3), 319–412.

Sergeev, V., R. Elphic, F. Mozer, A. Saint-Marc, and J. Sauvaud (1992), A two-satellite study of nightside flux transfer events in the plasma sheet, *Planetary and space science*, *40*(11), 1551–1572.

Sergeev, V., V. Angelopoulos, C. Carlson, and P. Sutcliffe (1998), Current sheet measurements within a flapping plasma sheet, *Journal of Geophysical Research: Space Physics*, *103*(A5), 9177–9187.

Sergeev, V., A. Runov, W. Baumjohann, R. Nakamura, T. Zhang, M. Volwerk, A. Balogh, H. Reme, J. Sauvaud, M. André, et al. (2003), Current sheet flapping motion and structure observed by cluster, *Geophysical research letters*, *30*(6).

Slavin, J., B. Tsurutani, E. Smith, D. Jones, and D. Sibeck (1983), Average configuration of the distant (¡ 220 re) magnetotail: Initial ISEE-3 magnetic field results, *Geophysical research letters*, *10*(10), 973–976.

Slavin, J., E. Smith, B. Tsurutani, D. Sibeck, H. Singer, D. Baker, J. Gosling, E. Hones, and F. Scarf (1984), Substorm associated traveling compression regions in the distant tail: ISEE-3 Geotail observations, *Geophysical research letters*, *11*(7), 657–660.

Sweet, P. A. (1958), 14. the neutral point theory of solar flares, in *Symposium-International Astronomical Union*, vol. 6, pp. 123–134, Cambridge Univ Press.

Torbert, R., C. Russell, W. Magnes, R. Ergun, P.-A. Lindqvist, O. LeContel, H. Vaith, J. Macri, S. Myers, D. Rau, et al. (2016), The fields instrument suite on MMS: Scientific objectives, measurements, and data products, *Space Science Reviews*, *199*(1-4), 105–135.

Treumann, R., C. Jaroschek, O. Constantinescu, R. Nakamura, O. Pokhotelov, and E. Georgescu (2004), The strange physics of low frequency mirror mode turbulence in the high temperature plasma of the magnetosheath, *Nonlinear Processes in Geophysics*, *11*(5/6), 647–657.

Tsurutani, B., E. Smith, R. Anderson, K. Ogilvie, J. Scudder, D. Baker, and S. Bame (1982), Lion roars and nonoscillatory drift mirror waves in the magnetosheath, *Journal of Geophysical Research: Space Physics*, *87*(A8), 6060–6072.

Tsyganenko, N. (1989), A magnetospheric magnetic field model with a warped tail current sheet, *Planetary and Space Science*, *37*(1), 5–20.

Walsh, B., T. Phan, D. Sibeck, and V. Souza (2014a), The plasmaspheric plume and magnetopause reconnection, *Geophysical Research Letters*, *41*(2), 223–228.

Walsh, B., J. Foster, P. Erickson, and D. Sibeck (2014b), Simultaneous ground-and space-based observations of the plasmaspheric plume and reconnection, *Science*, *343*(6175), 1122–1125.

Wiltberger, M., V. Merkin, J. G. Lyon, and S. Ohtani (2015), High-resolution global magnetohydrodynamic simulation of bursty bulk flows, *Journal of Geophysical Research (Space Physics)*, *120*, 4555–4566, doi: 10.1002/2015JA021080.